

BiomedGPT: A Unified Biomedical Generative Pre-trained Transformer for Vision, Language, and Multimodal Tasks

Kai Zhang¹, Jun Yu¹, Eashan Adhikarla¹, Rong Zhou¹, Zhiling Yan¹, Yixin Liu¹, Zhengliang Liu¹⁰, Lifang He¹, Brian Davison¹, Xiang Li², Hui Ren², Sunyang Fu³, James Zou^{4,12}, Wei Liu⁵, Jing Huang^{6,7}, Chen Chen⁸, Yuyin Zhou⁹, Tianming Liu¹⁰, Xun Chen¹¹, Yong Chen⁶, Quanzheng Li², Hongfang Liu³, and Lichao Sun^{1*}

¹Department of Computer Science and Engineering, Lehigh University, PA

²Department of Radiology, Massachusetts General Hospital and Harvard Medical School, MA

³McWilliams School of Biomedical Informatics, UTHealth Houston, TX

⁴Department of Biomedical Data Science, Stanford University School of Medicine, CA

⁵Department of Radiation Oncology, Mayo Clinic, FL

⁶Department of Biostatistics, Epidemiology, and Informatics, University of Pennsylvania, PA

⁷PolicyLab, Children's Hospital of Philadelphia, PA

⁸Department of Computer Science, University of Central Florida, FL

⁹Department of Computer Science and Engineering, University of California, Santa Cruz, CA

¹⁰School of Computing, University of Georgia, GA

¹¹Knox Advanced R&D, Samsung Research America, CA

¹²Department of Computer Science, Stanford University, CA

*To whom the correspondence should be addressed.

Abstract

Conventional task- and modality-specific artificial intelligence (AI) models are inflexible in real-world deployment and maintenance for biomedicine. At the same time, the growing availability of biomedical data, coupled with the advancements in modern multi-modal multi-task AI techniques, has paved the way for the emergence of generalist biomedical AI solutions. These solutions hold the potential to interpret different medical modalities and produce expressive outputs such as free-text reports or disease diagnosis. Here, we propose BiomedGPT, the first open-source and generalist visual language AI for diverse biomedical tasks. BiomedGPT achieved 16 state-of-the-art results across five clinically significant tasks on 26 datasets. Notably, it outperformed OpenAI's GPT-4 with vision (GPT-4V) in radiology human evaluation and surpassed Google's Med-PaLM M (12B) in breast cancer diagnosis and medical visual question answering. Moreover, BiomedGPT facilitates zero-shot transfer learning, greatly enhancing its utility as a biomedical assistant, similar to ChatGPT. Our method demonstrates effective training with diverse datasets can lead to more practical biomedical AI.

1 Introduction

Artificial intelligence (AI) techniques, especially transformer-based foundation models, have emerged as a powerful tool for solving a wide range of challenges within biomedicine [1, 2, 3, 4, 5]. These span from radiograph interpretation [6, 7], clinical information summarization [8, 9], and precise disease diagnostics [10, 11]. However, many of today's biomedical models act as specialist systems, often tailored for specific tasks, modalities, or particular anatomical regions [12].

In the context of clinical decision-making, such a specialized approach may have limitations and biases due to potential information loss. For example, identifying the most suitable treatment plans for older adults with

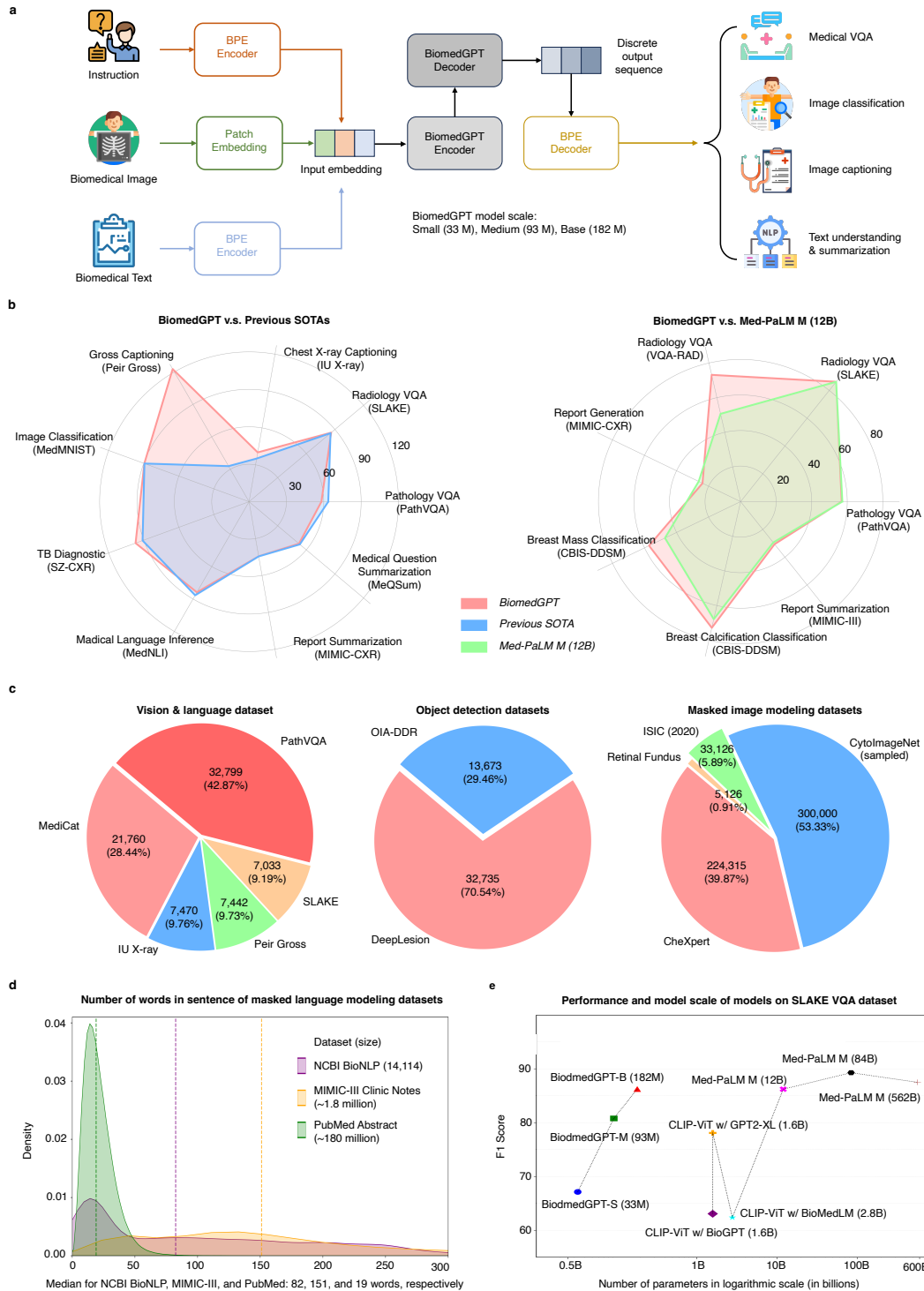


Figure 1: The overview of BiomedGPT: workflow, performance and pretraining datasets. **(a)** Graphical illustration of how BiomedGPT handle multi-modal inputs and perform diverse downstream tasks. The expected form of output for each task is determined by feeding the specific instruction to the model. **(b)** Comparative performance analysis: this figure contrasts the achievements of BiomedGPT with prior SOTA results and Med-PaLM M (12B). The evaluation metrics include: accuracy for image classification, medical language inference, and visual question answering (VQA) (benchmarked against SOTA results); CIDEr for image captioning; ROUGE-L for text summarization; weighted F1 scores for VQA (in comparison with Med-PaLM M); and F1-macro for breast mass and calcification classification (also in comparison with Med-PaLM M). **(c)** Distribution of pretraining datasets including image captioning and VQA as vision & language dataset, object detection datasets, and image-only datasets for masked image modeling. **(d)** Density plot of the number of words per sentence in the text-only pretraining datasets. **(e)** Scale-related performance comparison: BiomedGPT exhibits superior performance on the SLAKE VQA dataset, even with significantly fewer parameters than its counterparts.

multiple chronic conditions (MCCs) involves considering a complex set of disease patterns, which requires a collaborative and holistic care approach [13]. Another motivation for shifting specialization to generalization is the national priority of patient-centered care, which involves providing care that aligns with patients' values and preferences [14, 15]. One conceptual model that exemplifies patient-centered care is the Patient Priorities Care model [13, 16]. This model prioritizes care that aligns with patients' values and preferences, and it places active patient engagement at its core. These approaches emphasize the importance of shifting the focus of care from disease-specific outcomes or survival to a patient-oriented perspective. Therefore, when designing AI models, there is a compelling need to integrate information across various tasks and modalities and enhance existing AI techniques to better align with patient-centeredness.

Unified and generalist AI models, capable of handling multiple tasks and modalities across diverse domains within a singular architecture, offer fresh potential to draw a comprehensive view of the patient for healthcare [17, 18, 19, 20, 21]. By learning universally valuable representations from the knowledge encoded in medical data, such models bring several practical benefits in medicine, including economical deployment of a single model for thousands of diseases, rapid pre-clinic diagnostics in emergencies, and enhanced generalization to rare symptoms. Implementing unified biomedical AI is challenging: the versatility requires comprehension of multi-domain datasets, standardization of multi-modal inputs/outputs, and diversity of training tasks. Until recently, few studies have explored fine-tuning the large language model (LLM) with a visual encoder to achieve a unified biomedical AI model. For example, Med-PaLM M integrates the Pathways Language Model (PaLM) with the Vision Transformer (ViT) [21, 22, 23]. This model undergoes fine-tuning on clinical language, imaging, and genomics using a unified set of weights, establishing Med-PaLM M as the largest medical vision-language model with an impressive 562 billion parameters [24]. However, due to its closed-source nature and data regulations such as HIPAA, it remains inaccessible for public use and broader assessment by healthcare institutions. Other models, generally integrating CLIP's visual encoder with LLM, are predominantly evaluated on vision-language tasks, specifically visual-question answering (VQA). They primarily showcase proficiency in managing multi-modal inputs, but not in navigating a wide array of tasks [25, 26, 27, 28].

In this paper, we introduce BiomedGPT, a unified model that was pre-trained on various types of biomedical data (**Fig. 1c and Fig. 1d**) paired with task-specific instructions, to address the above limitations. BiomedGPT is implemented as a sequence-to-sequence model with a BERT-style encoder over corrupted text and a GPT-style left-to-right autoregressive decoder (**Fig. 1a and Methods**) [29, 30, 31, 32, 33]. The architecture's design principle aims for the encoder to efficiently map various modalities into a consolidated semantic representation, while the decoder adeptly handles a wide array of tasks through generation [34]. To evaluate the adaptability and efficacy of BiomedGPT, we fine-tuned it on 25 curated datasets that encompass five pivotal medical AI tasks: disease classification (vision-only), medical language understanding, text summarization, image captioning/description and VQA. Our model achieves the state-of-the-art (SOTA) results in 15 out of 25 experiments (**Extended Table. 1**), which demonstrates its competitive performance against leading medical AI models, even with its lightweight of 182 million parameters — **66 times smaller** than the leanest Med-PaLM M at 12 billion (**Fig. 1b and Fig. 1e**). By harnessing the power of BiomedGPT to analyze intricate data, there lies transformative potential for its integration into the broader healthcare ecosystem to improve patient care, hospital operations, and medical education.

Our first key contribution is the development of BiomedGPT, a fully open-source and lightweight generalist biomedical AI model. Despite its relatively compact size of just from 33 to 182 million parameters, BiomedGPT delivers SOTA results across a range of datasets and excels in five distinct tasks. By fully open-sourcing, we ensure that both the model checkpoint and our entire training process, including detailed data preprocessing workflows and codes, are readily accessible to the public. In contrast, related works such as Med-PaLM M and GPT-4V either not provide access for usage or not explicitly explain the training data and techniques. This transparency not only facilitates replication and verification of our work but also serves as a valuable resource for advancing research in the biomedical AI field.

The next contribution is the successful deployment and evaluation of BiomedGPT in a real-world healthcare setting. We provided clear and detailed guidance to the technical team at Massachusetts General Hospital for the deployment, fine-tuning, and inference of our model, ensuring a seamless and straightforward workflow. Further enhancing the practical value of our work, we conducted an evaluation with radiologists

to assess the accuracy and reliability of AI-generated answers for questions related to chest X-ray images. The outcomes of the radiologist assessment demonstrated promising results, surpassing GPT-4 with vision (GPT-4V) [35] by a significant margin (refer to **Results**), indicating the potential of BiomedGPT as a supportive tool in medical diagnostics and decision-making.

Finally, in our paper (see **Discussion**), we thoroughly discuss the significant challenges faced by unified and generalist models, as highlighted by our ablation study and the practical tests conducted during the deployment of our model. Our model's performance demonstrates the promising capabilities of unified models in biomedicine, yet it also underscores the necessity for significant improvements to ensure their effectiveness and practicality in real-world healthcare environments.

2 Results

2.1 Generative self-supervised pretraining with freely-available datasets

Generative self-supervised pretraining leverages extensive unlabeled data to capture its intrinsic distribution, facilitating broad downstream applications in medicine [36, 37, 38, 39]. To maximize the generalization of our biomedical representations, we sourced from 14 freely-available datasets (**Fig. 1c**), ensuring the diversity of modalities (*i.e.*, medical imaging techniques like CT, and clinical texts like radiology report) and anatomy (*i.e.*, body parts). Our pretraining corpus contains 352,567 images, roughly 183 million text sentences, 46,408 object-label pairs, and 271,803 image-text pairs. We employed five prevalent pretraining tasks (see **Methods** for details): image-only (masked image modeling), text-only (masked language modeling), and multi-modal tasks like image captioning and VQA. We employed the OFA model [33], pre-trained on broad-domain data, as a starting point to infuse both general and medical expertise into BiomedGPT. In addition, to investigate how BiomedGPT performs across varying scales, we specifically introduced three versions of the model: BiomedGPT-S, BiomedGPT-M, and BiomedGPT-B, which correspond to small, medium, and base sizes, respectively (**Fig. 1a**).

2.2 Instruction-aware fine-tuning for downstream tasks

Multitasking is fundamental to a holistic and generalist model. Drawing inspiration from prior work on language models that utilize prompt/instruction learning and established unified frameworks aiming to avoid task-specific modules [32, 40, 41, 42, 43], we defined each task using a manually crafted instruction, with VQA as the sole exception that relies on the questions themselves to guide the model (**Methods and Extended Table 2**). Our selection of downstream tasks stemmed from their potential real-world applications: medical image classification often aids in disease diagnostics; text understanding and generation can streamline hospital operations by easing doctors' report-writing burdens, and also facilitate medical education, offering condensed key insights from reports or articles. Furthermore, image captioning and VQA lay the groundwork for future healthcare chatbots, addressing challenges where common language might be ambiguous, but medical terminologies are too hard for most people to understand.

2.3 BiomedGPT exhibits competitive performance as a lightweight model in multi-modal tasks

We fine-tuned BiomedGPT on two primary multi-modal tasks, namely, VQA and image captioning, each using three downstream datasets. The VQA datasets included radiology data covering five different anatomies (VQA-RAD [44] and SLAKE [45]), in addition to pathology data that captures both bodily and tissue-specific details (PathVQA [46]). For captioning, we incorporated Chest X-ray datasets (IU X-RAY [47] and MIMIC-CXR [48]) as well as clinical photographs from PEIR GROSS [49]. For comparison, we benchmarked BiomedGPT against leading models for each dataset. The results for the SOTA models were taken from the original paper due to the substantial computing resources necessary for replicating such a leading model. This is often because they are typically large-scale and lack readily available model checkpoints for inference.

We evaluated our model's VQA performance by comparing generated answers with the ground truths. Our primary metric of interest was the weighted F1 score, which harmonizes precision and recall, thereby accommodating answer imbalances. Additionally, we dissected the accuracy of both "closed-ended" and "open-ended" question-answer pairs. While the former presents limited multiple-choice answers, the latter necessitates free-form text responses. Our 182-million parameter model, BiomedGPT-B for short, was compared with the extensive 12-billion parameter Med-PaLM M (or Med-PaLM M (12B)). Remarkably, even

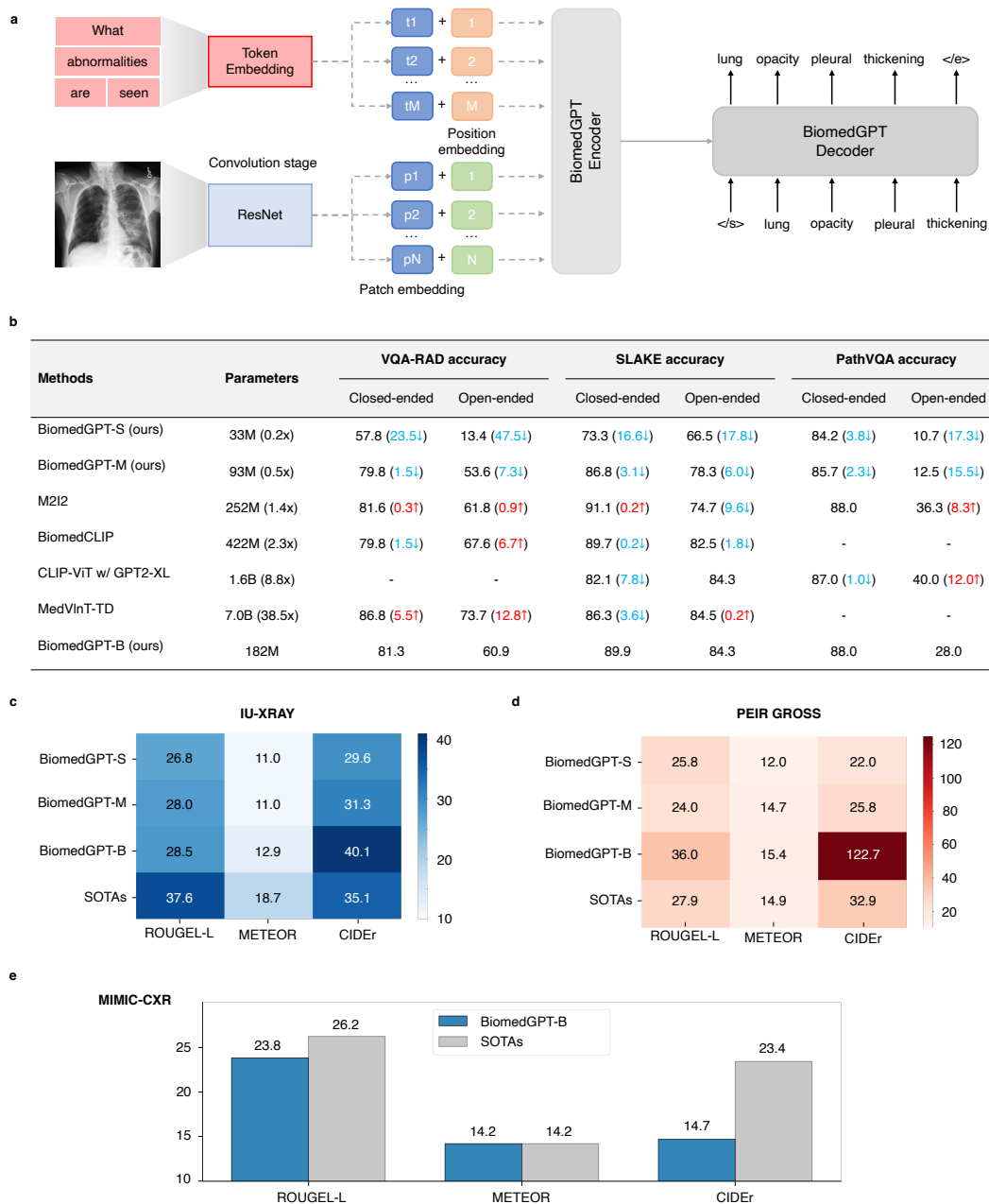


Figure 2: BiomedGPT performs fine-tuning for vision-language downstream tasks. **(a)** Graphical illustration of inference workflow of BiomedGPT for VQA task. Our model can discrete both visual and linguistic inputs from questions into tokens and generated the corresponding answers. **(b)** VQA performance of BiomedGPT and the leading models in terms of closed-ended and open-ended accuracies. **(c)** Image captioning performance of BiomedGPT and SOTAs on the IU-XRAY data. The evaluation metrics are ROUGEL-L, METEOR and CIDEr. **(d)** Image captioning performance of BiomedGPT and SOTAs on the PEIR GROSS data. **(e)** Image captioning performance of BiomedGPT-B and SOTAs on the MIMIC-CXR.

with the much smaller model size, BiomedGPT-B achieved impressive outcomes (**Fig. 1b**). On the VQA-RAD and SLAKE datasets, BiomedGPT-B achieved F1 scores of 73.2% and 85.24%, respectively. This represents a significant increase of 22.5% on VQA-RAD and a slight improvement of 0.02% on SLAKE, compared to the Med-PaLM M (12B) model. Additionally, on the PathVQA dataset, BiomedGPT-B scored an F1 of 56.9%, just 0.4% lower than Med-PaLM M, while utilizing a model with 98.5% fewer parameters.

A deeper dive into closed- and open-ended VQAs, visualized in **Fig. 2b**, revealed nuanced findings. On the SLAKE dataset, BiomedGPT-B noted an 89.9% closed-ended accuracy, down by 1.1% compared to the M2I2 model. However, in open-ended scenarios, our model flourished with an 84.3% accuracy, overshadowing M2I2's 74.7%. On the other hand, for VQA-RAD and PathVQA datasets, BiomedGPT fell short of the reigning state-of-the-art standards, primarily due to its performance on open-ended queries: 60.9% and 28.0%, respectively. This discrepancy can be linked to BiomedGPT's compact model scale, as illustrated in **Fig. 2b**, and the competitors leveraging more extensive VQA datasets during pretraining, as noted in [50, 51, 52, 53]. Despite this, our model clocked in promising closed-ended accuracies: 88.0% on PathVQA (up by 1.0% compared to the existing SOTA model built on CLIP and GPT-2 [53]) and 81.3% on VQA-RAD (down by 5.5% compared to MedVInT-TD [51]). The overall accuracy of our BiomedGPT model is detailed in **Extended Table. 1**. Notably, BiomedGPT achieved an 86.1% overall accuracy on SLAKE dataset, surpassing the previous SOTA performance of 85.4% set by BiomedCLIP [52].

For image captioning, we meticulously assessed the quality of machine-generated text using three metrics: ROUGE-L [54], METEOR [55], and CIDEr [56]. These metrics measure text fluency and order, recognize synonyms and word stems, and prioritize significant image objects over non-informative words, respectively [57]. In which, CIDEr is specifically designed for evaluating textual descriptions of images, is therefore utilized as the primary metric in both our validation and testing phases. On the PEIR GROSS dataset (see **Fig. 2d**), our BiomedGPT model outperformed the existing SOTA benchmark [58], yielding enhancements of 8.1%, 0.5%, and 89.8 in ROUGE-L, METEOR, and CIDEr metrics, respectively. In contrast, on the IU X-RAY dataset (**Fig. 2c**), while BiomedGPT achieved a leading CIDEr score of 40.1 (an improvement of 5.0 over the SOTA model), it registered lower scores in METEOR and ROUGE-L, at 12.9% (a decline of 5.8% against the top model [59]) and 28.5% (a 9.1% drop compared to the benchmark [60]), respectively. These results arise from our model selection during training. Specifically, we aimed for the model to capture key points from the image, selecting the checkpoint with the highest CIDEr on validation data for test data inference. On the MIMIC-CXR dataset **Fig. 2e**, in terms of METEOR, our model matched the leading model [59] with a score of 14.2%. However, it fell short of the larger SOTA model, Med-PaLM M (12B), scoring 23.7% in ROUGE-L (a decrease of 2.5%) and 14.7 in CIDEr (down by 8.7).

2.4 BiomedGPT enables accurate medical image classification

We selected nine image subsets from MedMNIST [61], encompassing seven modalities and three views of Abdominal CT scans: (1) colon pathology with nine tissue types; (2) dermatoscopy images of seven typical pigmented skin lesions; (3) breast ultrasound (normal, benign, and malignant); (4) retinal OCT categorized into four types of retinal diseases; (5) chest X-Ray images for binary-class classification of pneumonia against normal; (6) blood cell microscope showcasing eight kinds of normal cells; (7)-(9) Abdominal CT with 11 body organs across axial, coronal, and sagittal views. Additionally, we tested the model on two high-resolution pulmonary disease datasets, with a specific focus on pulmonary tuberculosis (TB), which has a limited number of samples: (10) Montgomery County chest X-ray set (MC-CXR) with the size of either 4,020×4,892 or 4,892×4,020 pixels; (11) Shenzhen chest X-ray set (SZ-CXR) with approximate dimensions of 3K×3K pixels. Given that these datasets are class-balanced and provide easy comparison with prior work, we employed top-1 accuracy for evaluation. As shown in **Fig. 3a-c**, BiomedGPT outperformed on 8 of the 11 datasets.

Notably, on the SZ-CXR and MC-CXR datasets [62] (binary classification), BiomedGPT posted accuracies of 97.0% and 89.7%, reflecting improvements of 6.0% and 0.8% over the previously leading model – LightTBNNet [63], respectively. For MedMNIST, BiomedGPT achieved 6 out of 9 best accuracies compared to the existing methods, specifically 1.2% improvement in average on datasets (4)-(9), and 2.1% decrease

in average on datasets (1)-(3).

Considering the model scale, it becomes evident that BiomedGPT exhibits significant performance enhancements on high-resolution datasets as its scale increases (**Fig. 3d**). Specifically, on the MC-CXR dataset: the small model logged an 75.9% accuracy. In contrast, the medium model showcased a score of 82.8% that is 6.9% higher than its smaller counterpart, and the base model continued this upward trajectory with a score of 89.7% surpassing the medium model by 6.9%. On the SZ-CXR dataset, the small model registered an accuracy of 83.5% while the medium model displayed a significant enhancement with a 13.5% improvement, and the base model showcased its capability with a 12.8% improvement over the small model's performance. However, on the lower-resolution MedMNIST datasets, the growth was more conservative. Compared to the small model, the medium and base versions achieved incremental improvements, averaging at just 2% and 2.3% respectively.

Additionally, we benchmarked our BiomedGPT against Med-PaLM M on the CBIS-DDSM dataset [64] for both 3-class lesion-level mass classification and calcification classification. Using the F1-Macro as the evaluation metric, consistent with the methodology employed in the Med-PaLM studies, we found that BiomedGPT-B outperforms all versions of Med-PaLM M, spanning 12B, 84B, and 584B parameters (**Fig. 3c and Extended Fig. 2**). Specifically, BiomedGPT-B achieved an F1-Macro score of 57.2% in mass classification, surpassing the highest score of Med-PaLM M (562B) at 51.1%. Furthermore, for calcification classification, BiomedGPT-B registered a score of 72.8%, besting the top-performing Med-PaLM M (12B) which managed a score of 67.9%. These findings underscore the impressive efficiency and efficacy of BiomedGPT, even when squared against models of larger scales. It's a testament to the optimization and the potential that our model brings to the medical imaging analysis, showing that performance gains are achievable without resorting to excessively large-scale models.

2.5 BiomedGPT can handle clinical text understanding and generation

We conducted an evaluation of BiomedGPT's capabilities in language processing by focusing on two critical tasks: (1) medical natural language inference/understanding, utilizing the MedNLI dataset [65], which tests the model's comprehension in deducing hypotheses from provided premises; (2) medical text summarization, applied to datasets of doctor-patient dialogues (MedQSum [66] and HealthCareMagic [67]) as well as radiology reports (MIMIC-CXR [48] and MIMIC-III [68]). These tasks are designed to assess the model's proficiency in understanding and condensing complex medical narratives that holds tremendous potential for real-world medical applications. For instance, BiomedGPT can potentially help reduce clinician's administrative burden by assisting clinical information summarization and organization.

In the evaluation of the MedNLI dataset for 3-class classification (entailment, contradiction, or neutral), we adopted accuracy as our evaluation metric, consistent with prior research (**Fig. 3f**). Our findings reveal that the scaling law remains applicable to tasks solely focused on language, as evidenced by the progressive accuracy gains across the three BiomedGPT model variants: 75.8%, 80.8%, and 83.8% corresponding to increases in model size. Notably, when compared to the state-of-the-art performance of SciFive-Large at 86.6% accuracy, our BiomedGPT-B, with merely a quarter of SciFive-Large's parameter count, exhibited a modest decline in accuracy of only 2.8%. It is also important to acknowledge that our pretraining corpus was limited in scale relative to the comprehensive corpus utilized by SciFive, which includes the Colossal Clean Crawled Corpus [69], PubMed abstracts¹, and full-text articles from PubMed Central². Considering significant data processing and computing demands for the unified model, we utilized only a subset of the PubMed abstracts.

In evaluating text summarization, we employed the ROUGE-L metric to assess BiomedGPT-B's performance across four benchmark datasets (**Fig. 3e**). BiomedGPT-B demonstrated its capability in summarizing doctor-patient dialogues on the MedQSum and HealthCareMagic datasets, achieving ROUGE-L

¹<https://pubmed.ncbi.nlm.nih.gov>

²<https://www.ncbi.nlm.nih.gov/pmc>

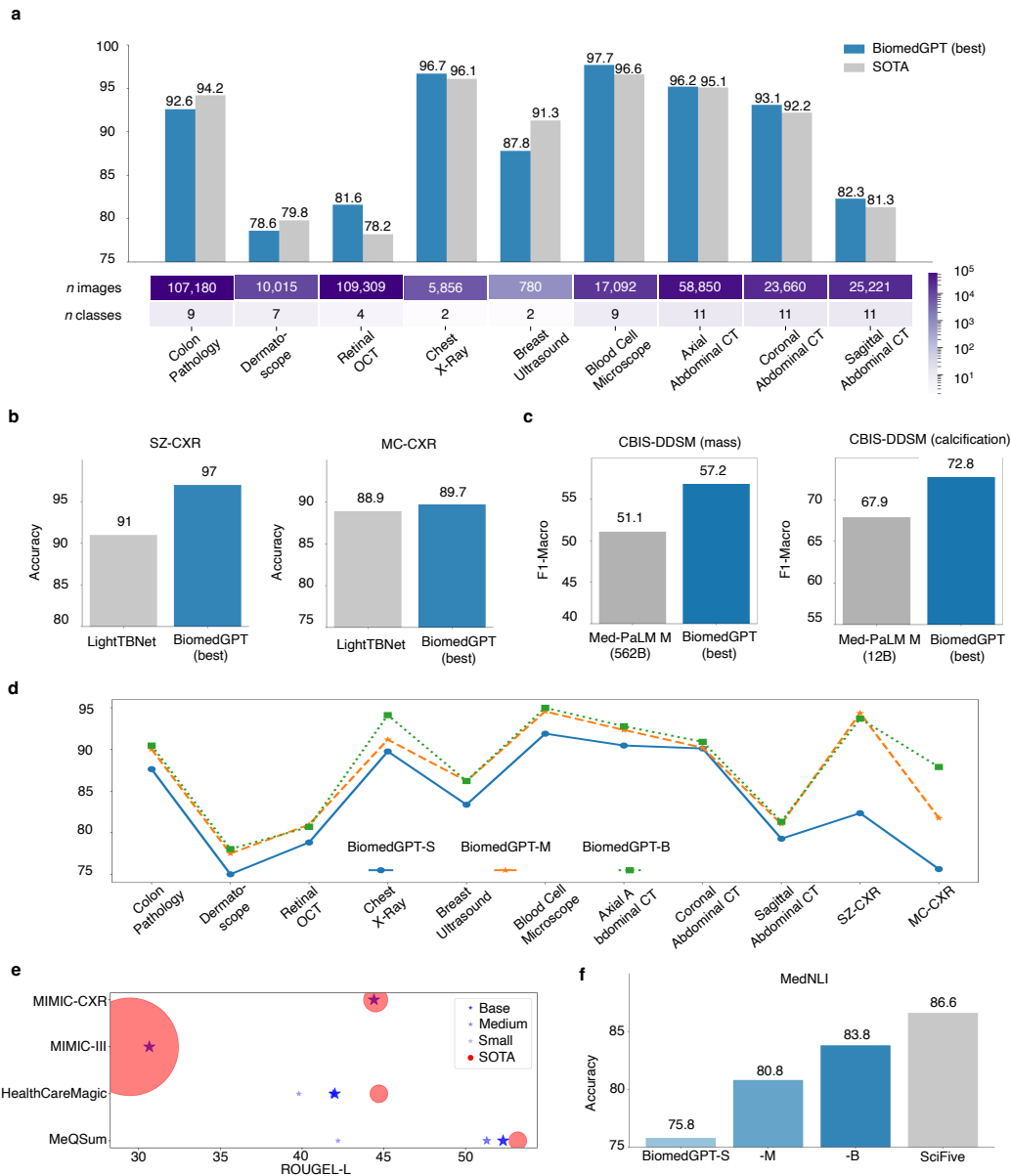


Figure 3: BiomedGPT performs fine-tuning for uni-modal downstream tasks. **(a)** Evaluation of the MedMNIST dataset within each domain type. **(b)** Image classification performances with accuracy across two high-resolution image datasets. Note that on SZ-CXR, BiomedGPT-M showed the best performance. **(c)** Image classification performance with F1-Macro on CBIS-DDSM dataset. **(d)** Accuracies across 11 datasets in terms of model scales. In general, larger models tend to perform better. **(e)** ROUGE-L across four text summarization datasets in terms of model scales. The size of legends represent the number of parameters. **(f)** Medical language inference and understanding performances on MedNLI regarding model scales.

scores of 52.3% and 42%, respectively. When compared to leading models [70, 71] with 400 million parameters that recorded ROUGE-L scores of 53.2% and 44.7%, BiomedGPT-B showed only minor performance drops of 0.9% and 2.7%. Additionally, in summarizing radiology reports, specifically in generating impressions from radiologists' findings, BiomedGPT-B achieved a ROUGE-L score of 44.4% on the MIMIC-CXR dataset. This result is closely aligned with the state-of-the-art, trailing by a mere 0.1% from the top score of 44.5% [9]. In the MIMIC-III dataset, BiomedGPT-B's performance stood out with a ROUGE-L score of 30.7%, surpassing Med-PaLM M (12B) which scored 29.5%. This underscores the competitive edge of BiomedGPT-B considering its parameter economy.

2.6 Pretraining tasks influence downstream efficacy

To gain a deeper understanding of the impact of individual pre-training tasks on downstream performance, we implemented an ablation study that involved systematically excluding image-only or text-only task during pre-training and subsequently fine-tuning the resultant models on five downstream tasks. To ensure a fair comparison, we utilized downstream datasets that were excluded from the pre-training phase: (1) PneumoniaMNIST [61] for image classification; (2) ROCO [72] for image captioning; (3) VQA-RAD for VQA; (4) MeQSum for text summarization; (5) MedNLI for text understanding. Moreover, each model was fine-tuned using the consistent training receipts across the same datasets.

Due to the limited computing resources, we performed this study using BiomedGPT-S only. For short, we denote the pretraining without using masked image modeling, without using masked language modeling, and without using object detection as *w/o MIM* and *w/o MLM*, respectively. Referring to **Fig. 4a**, we used the BiomedGPT-S model, pre-trained with all tasks, as the baseline. This model reached a 91.8% accuracy in image classification, a ROUGE-L score of 42.2% in summarization, 69.3% in text understanding accuracy, a CIDEr score of 13.2 for image captioning, and 37.5% in VQA accuracy (as shown in **Fig. 4b**).

When the masked image modeling component was excluded, a decline in performance was noted for image-centric and multimodal tasks after fine-tuning (**Fig. 4b**), such as a 3.5% drop in image classification accuracy (down to 88.3%), a decrease of 1.0 in CIDEr for captioning (to 12.2), and a 4.0% decrease in VQA accuracy (to 33.5%). Contrarily, an improvement was observed in text-centric tasks; the model without MIM attained a 2.1% increase in ROUGE-L for summarization (to 44.3%) and a 0.6% increase in text understanding accuracy (to 69.9%). These results suggest that Masked Image Modeling has no bearing on text-only tasks, which could account for the observed enhancements.

When masked language modeling was not included during pre-training, we observed a decline in performance across all tasks in downstream evaluation (**Fig. 4b**). This was evidenced by a 4.8% decline in image classification accuracy, falling to 87.0%, and a CIDEr score drop by 1.2 point for image captioning, taking it down to 12.0. There was also a 5.1% reduction in VQA accuracy, which decreased to 32.4%. For text-centric tasks, the absence of MLM led to a much worse outcome for text summarization, seeing a 23.1% decrease in ROUGE-L score, downing to 19.1% only, and text understanding accuracy is also degraded by 0.7%, settling at 68.6%. Such a phenomenon showed the significance of masked language modeling for a unified model. Even for the image-only tasks like image classification, we still need a dictionary of text tokens for label generation.

The exclusion of object detection from the pretraining phase resulted in relatively noticeable performance reductions in downstream tasks like image classification and radiology captioning (**Fig. 4b**). Notably, the model's accuracy on PneumoniaMNIST dropped to 88.3%, compared to 91.8% achieved by BiomedGPT-S, and its CIDEr score for radiology captioning decreased to 12.7 from the 13.2 scored by BiomedGPT-S. However, for the other three datasets, the performance changes were relatively minor. This could be attributed to both the limited number of object detection samples involved in our study and the task's somewhat tenuous connection to language-only tasks.

In summary, our study highlights the importance of task diversity in pre-training for the unified medical AI.

While the exclusion of image-specific tasks might benefit performance on text-only downstreams, a varied task regime is vital for maintaining generalization across both unimodal and multimodal applications. For instance, the comprehensive pre-training of BiomedGPT-S across all tasks yielded superior outcomes on three out of five tasks when compared to its counterparts (Fig. 4b), as revealed in our ablation study.

2.7 Diversity of pretraining datasets enhance model’s ability

Additional evaluations were conducted to address the query: “Can the proposed model handle unseen data modalities (e.g., images from a new different imaging device like an ultrasound)?” To investigate this, we adjusted our dataset selection for both pretraining and downstream tasks (Fig. 4d). Specifically, we’ve drawn 3,489 and 6,461 chest X-ray image-text pairs from SLAKE and IU X-ray datasets, respectively. Additionally, we selected an equal quantity of images (7,452) from CheXpert while disabling masked language modeling and object detection during pretraining for simplification (Fig. 4c). The pre-trained BiomedGPT on x-ray modality, denoted as *RadGPT-{size}*, is subsequently fine-tuned on radiology-related datasets: chest x-ray, breast ultrasound and liver CT (coronal-view) from MedMNIST. As a comparative baseline, we selected ResNet-50 [73], which was trained from scratch on these three datasets (Fig. 4e). This choice was informed by its efficacy in prior studies [61]. We observed an impressive in-domain transferability of BiomedGPT from the outcome, specifically, RadGPT-B outperformed the baseline, achieving 93.0% classification accuracy on the chest x-ray images, gaining 7.6% improvement. Furthermore, our results indicated that RadGPT maintain strong performance with out-of-domain modalities when the subjects of the medical imaging are anatomically adjacent, such as chest versus breast. For instance, on the breast ultrasound dataset, BiomedGPT-B achieved 90.4% accuracy which is significantly higher than the baseline’s 81.2%. However, for liver CT scans, we observed a necessity to scale up the model to attain comparable results to the baseline. In this case, RadGPT-B achieved 74.5% accuracy, which is 2.5% lower than the baseline’s 77.0%. Furthermore, our smaller and medium-sized BiomedGPT models only reached accuracies of 66.5% and 71.2% respectively, indicating decrease of 10.5 and 5.8 percentage points. This highlights the challenges in domain adaptation for medical applications when the pre-trained model does not learn diverse medical knowledge.

We further explored the aspect of cross-domain transferability. Specifically, We fine-tuned the aforementioned pre-trained model, RadGPT, using datasets from other domains such as blood cell microscopy and dermoscopy for image classification. Additionally, we selected MRI-only and CT-only image-text pairs from SLAKE, and conducted VQA fine-tuning. The results compared to the benchmark (the original BiomedGPT-B pre-trained with all modalities), measured in terms of accuracy, are presented in Fig. 4f. We found that cross-modality transfer with our model is feasible, albeit with potentially significant performance degradation. For example, RadGPT-B exhibited a notable decrease in accuracy compared to the baseline on both the DermaMNIST dataset (dermoscopy), with an 8.1% drop, and the SLAKE-CT VQA dataset, with a more significant reduction of 15.2%. It’s noteworthy that we had to double the training epochs as compared to the previous fine-tuning with a pre-trained model encompassing all modalities (100 vs. 50). Therefore, we conclude that modality comprehensiveness is critical for a unified biomedical AI model to facilitate efficient knowledge transfer.

2.8 BiomedGPT can answer new questions in natural language regarding an image input without further training

In our study, we focused on evaluating the zero-shot capabilities of BiomedGPT in VQA, highlighting its ability to answer biomedical questions in a freeform manner at scale, without requiring retraining [74, 75, 32, 76, 77]. This contrasts sharply with earlier biomedical AI models, such as BERT-based or ViT-based models [78, 79, 80, 10, 81, 82] that depend on linear probing [83] and are incapable of zero-shot prediction, or CLIP-based models [77, 52, 84, 85, 86, 87] which necessitate predefined answer choices and generally only function effectively in limited-class image classification scenarios. Unlike these models, BiomedGPT

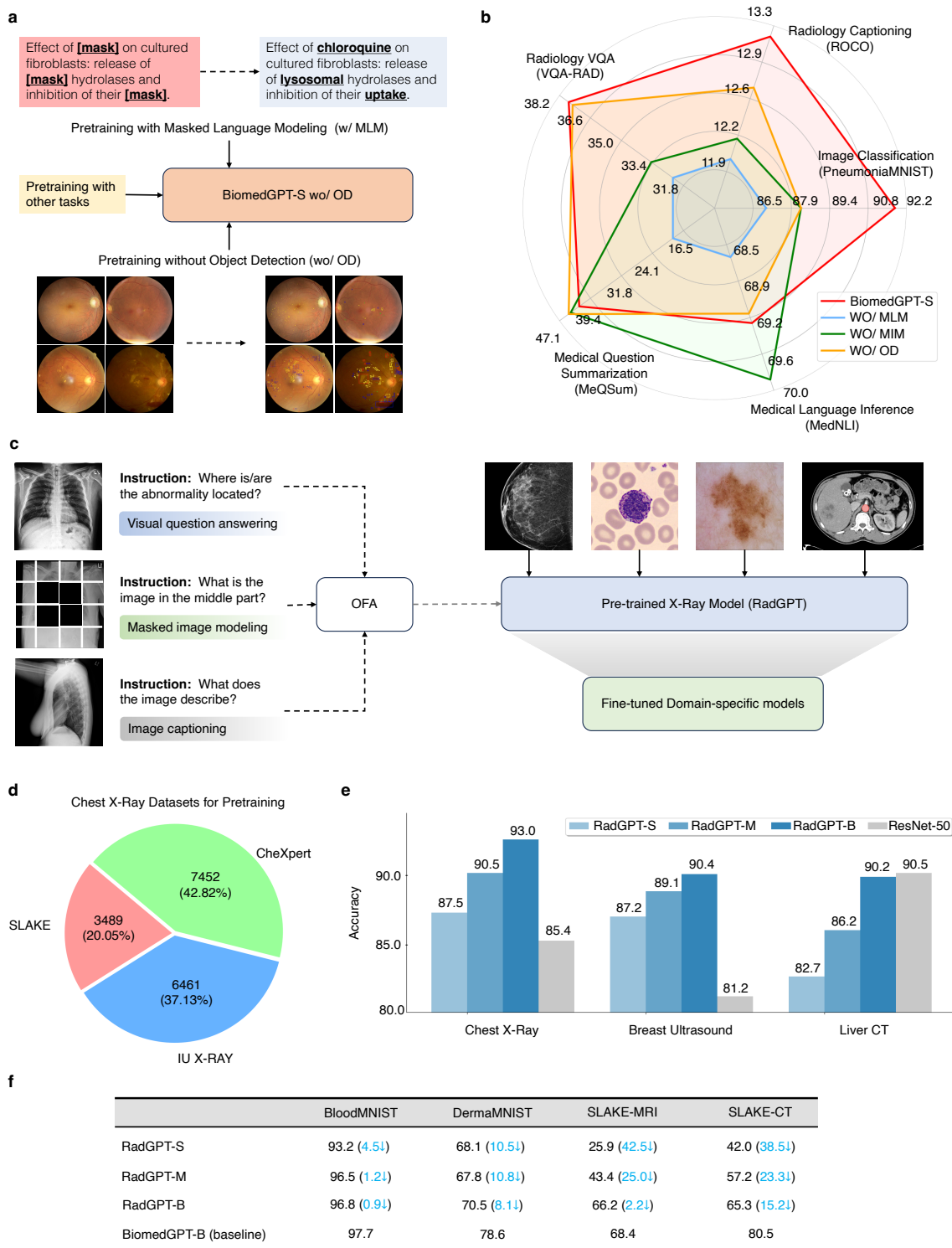


Figure 4: Ablation study to demonstrate the impact of diversity of pretraining datasets and tasks. **(a)** Descriptions of exclusion of object detection task and inclusion of MLM with other tasks in the pretraining. **(b)** Performance comparison excluding the specific task. Metrics used here are: accuracy for radiology VQA, medical language inference and image classification, CIDEr for radiology captioning, ROUGEL-L for medical question summarization. **(c)** Description of domain-specific (continual) pretraining with only chest X-ray datasets. The pre-trained model will be further used for fine-tuning on other domains. **(d)** Distribution of datasets for domain-specific pretraining. **(e)** In-domain transferability of BiomedGPT across three radiology modalities/datasets. **(f)** Cross-domain transferability of BiomedGPT across four datasets.

can autonomously generate answers by simply processing the input data, akin to how ChatGPT operates (Fig. 5a). This attribute of BiomedGPT marks a significant advancement in the field, offering more flexible and dynamic AI-driven solutions for biomedical inquiries.

While zero-shot prediction capabilities of pre-trained AI models might not be directly applicable in high-stakes industries like healthcare and medicine, they do provide insights into the models' foundational attributes. Better zero-shot performance suggests a more efficient and effective starting point for subsequent transfer learning, indicating the model's potential for fine-tuning to specific tasks in the medical field.

Automatic evaluation on zero-shot VQA presents challenges, primarily because (1) the model generates freeform answers that may not precisely match the gold-standard responses, and (2) programmatically determining the semantic relationship between the generated and gold answers isn't entirely reliable or trustworthy. To address this, we conducted our evaluation on a set of 39 representative VQA-RAD samples (absent from the pretraining data), drawn from the evaluation report [88] of GPT-4V [35] (the multimodal variant of ChatGPT), and manually assessed the accuracy of the generated answers. This evaluation aimed to determine whether BiomedGPT could match the performance of general-purpose multimodal models like the original OFA and GPT-4V, which is regarded as one of the most powerful multimodal models available. Our performance evaluation of BiomedGPT centered on two key metrics: (1) the accuracy of the model in providing correct answers, and (2) its ability to understand the questions and respond in a contextually relevant manner. Specifically, we measured accuracy to assess the model's precision in answering questions. For the second metric, we introduced the concept of *context-related accuracy*, where we evaluated whether the responses generated by the model accurately reflected the expected information from the question, regardless of whether the answers were technically correct or incorrect. This dual-focus approach allowed us to comprehensively assess both the factual correctness and contextual understanding capabilities of BiomedGPT in the zero-shot VQA domain.

In our study, we assessed the zero-shot accuracy of BiomedGPT across different model scales, comparing it with OFA models (large and base, featuring 470 and 182 million parameters, respectively) and GPT-4V, focusing on various question types as categorized by Yan et al. [88] (as shown in Fig. 5b and Extended Table 3). The findings, detailed in Fig. 5d, highlight BiomedGPT's reasonable capability in zero-shot learning for this intricate task. Specifically, the base version of BiomedGPT (BiomedGPT-B) correctly answered 19 out of 39 questions, a performance comparable to GPT-4V, which answered 20 correctly. GPT-4V demonstrated a stronger ability in recognizing imaging modalities (such as X-ray, CT), correctly answering 7 out of 8 questions (Fig. 5b). On the other hand, BiomedGPT showed a superior ability to assess object sizes within images, with BiomedGPT-B correctly answering 7 out of 11 questions and BiomedGPT-M answering 9 correctly. Furthermore, our analysis of the original OFA models on the dataset indicated that the large-scale version of OFA (OFA-L) correctly answered 14 questions, falling short of BiomedGPT-M's performance, which correctly answered 18 questions. The base-scale OFA (OFA-B) showed a comparable performance to BiomedGPT-S, with both achieving 11 correct answers. However, a significant challenge for both OFA variants was modality recognition, a fundamental aspect in accurately interpreting multimodal biomedical data. This finding underscores the importance of pretraining with biomedical data for enhanced zero-shot performance in this domain.

Regarding context-related accuracy (as shown in Fig. 5c), GPT-4V outperforms other models significantly. Specifically, it achieved a perfect score of 100% likely due to the advanced commercial GPT language models it is built upon [30, 31, 32, 89]. In comparison, the highest context-related accuracy achieved by BiomedGPT is 84.6%, with OFA models reaching 82.1%. The comparatively lower accuracy for OFA models and BiomedGPT-S largely stems from misunderstandings related to modality recognition (Extended Table 5, 6, and 7), which explains their challenges in accurately answering questions of this type (Fig. 5d). Meanwhile, BiomedGPT-B and BiomedGPT-M tend to misinterpret questions pertaining to structural identification and disease diagnosis (Extended Table 6), indicating specific areas where these models may require further refinement in pretraining to improve their understanding and response accuracy.

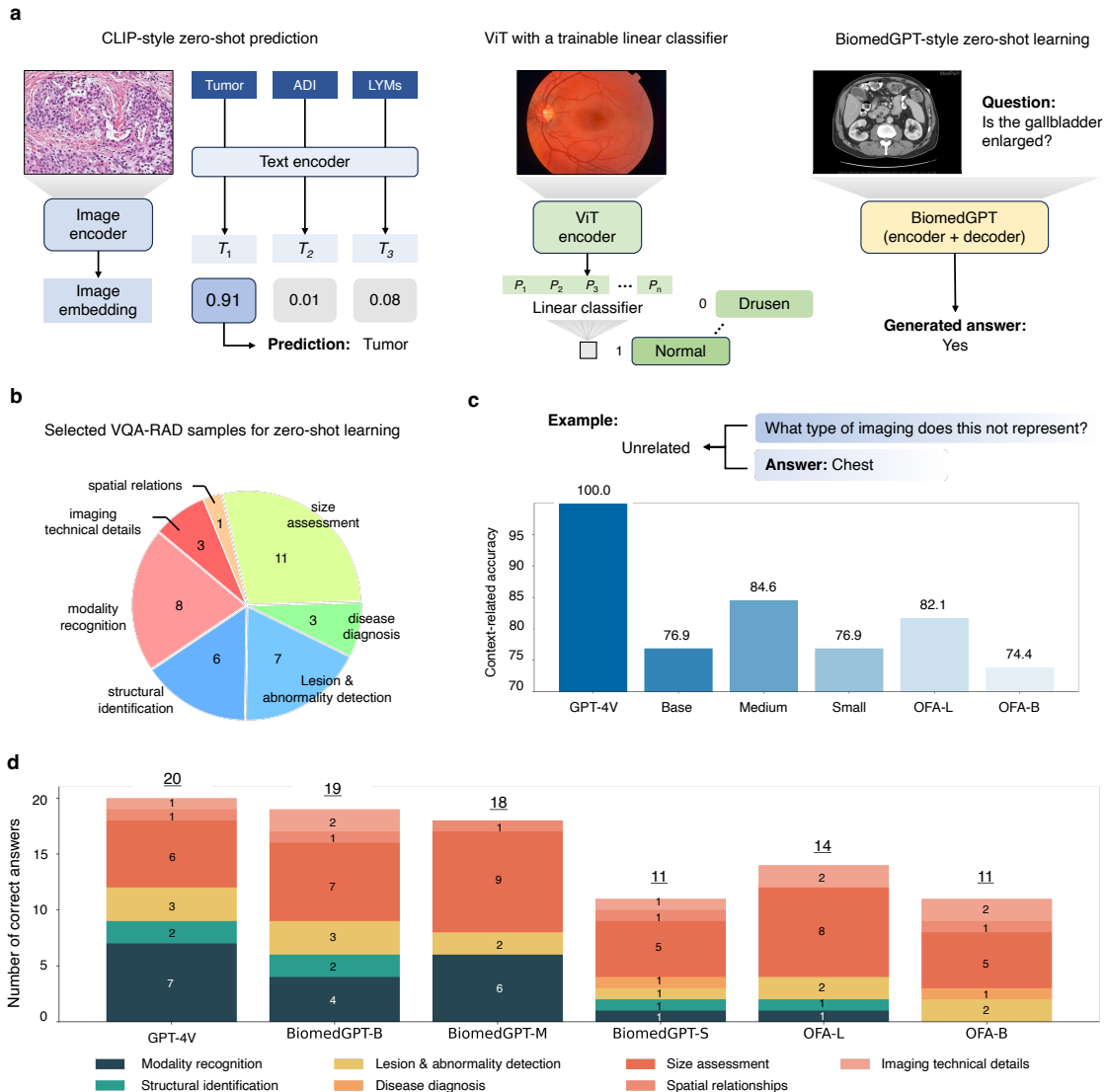


Figure 5: BiomedGPT generates the response via zero-shot transfer learning. **(a)** Graphical illustration of zero-shot classification using CLIP-style models, linear probing transfer learning using ViT or BERT-style models, and zero-shot generation of BiomedGPT. Notably, our model can generate the response without providing additional components such as the label candidates for CLIP or linear classifier requiring training for ViT. **(b)** Type distribution of the selected VQA-RAD samples for zero-shot evaluation. **(c)** Context-associated accuracy comparison among GPT-4V, BiomedGPT (base, medium, small) and OFL (large and base). We provide an example illustrating a mismatch between the generated answer and the question. Specifically, for a question asking about the “type of imaging,” the expected response should be along the lines of the imaging technique used, like X-ray, rather than the unrelated answer provided. **(d)** Zero-shot performances with the number of correct answers across 7 question types.

2.9 Human evaluation of BiomedGPT for radiology VQA

To further evaluate the clinical applicability and deployment challenges of BiomedGPT, we conducted a detailed analysis through radiologist evaluations of the model's generated responses to a wide range of questions. The responses were classified into four specific categories regarding accuracy and relevance: correct, partially correct, incorrect, and unrelated. This classification not only reflects the appropriateness of the answers but also their clinical severity, thereby providing a nuanced understanding of the model's potential utility in clinical practice. The details of human evaluation are described in the following:

Deployment setup. Our pre-trained BiomedGPT-B model was deployed by the system manager responsible for the computing cluster in Massachusetts General Hospital (MGH). It underwent fine-tuning with VQA samples derived from the MIMIC-CXR radiology reports, which constitute the official training set referenced in [90]. The selection of the model checkpoint post-fine-tuning was based on its accuracy performance on VQA samples, also sourced from official MIMIC-CXR validation set. The fine-tuning process took 27 hours and was executed on one NVIDIA A100-SXM4-40GB GPUs across 10 training epochs.

Evaluation procedure. To clinically evaluate the correctness of BiomedGPT's responses, we randomly selected 52 question-answer samples from 16 images in the official test set over six categories **Fig. 6a**: abnormality, presence, location, type, view, and severity level. We collected the answers generated by BiomedGPT and presented them to one seasoned radiologist at MGH for scoring (**Fig. 6b and 6c**). Additionally, the original radiology reports will be provided to the radiologist to serve as a reference, facilitating a potentially more precise evaluation. To further enhance our evaluation, we included an assessment of the answers generated by GPT-4V (**Fig. 6b & 6d and Supplementary**), widely recognized as one of the most powerful multi-modal foundation models developed by OpenAI. This allowed us to directly compare the performance of our BiomedGPT model against GPT-4V, providing a comprehensive understanding of our model's capabilities in relation to a leading AI system in the field.

Performance analysis. In our evaluation method, we categorized the generated answers as correct, partially correct, incorrect, or unrelated, and assigned them scores of 2, 1, 0, and -1, respectively. As depicted in **Fig. 6b**, BiomedGPT achieved an average score of 1.75 across all 52 samples, accumulating a total score of 91. In comparison, GPT-4V attained an average score of 1.17, resulting in a total score of 61. When considering the types of questions, BiomedGPT demonstrated superior performance in all five categories. Specifically, BiomedGPT achieved an average score of 1.62 to detect abnormalities, surpassing GPT-4V's average of 1.23 by a margin of 0.39. In the categories of presence-related and type-related questions, GPT-4V scored averages of 1.64 and 1.0, respectively, whereas BiomedGPT reached full credit with an average score of 2.0 in both categories, indicating improvements of 0.36 and 1.0, respectively. Notable performance disparities were also evident in localization and level-evaluation questions. BiomedGPT scored an average of 1.72 and 1.8 for these categories, significantly outperforming GPT-4V, which only managed 1.0 and 0.6, respectively (representing decreases of 0.72 and 1.2 points). However, for view-related questions, both AI systems achieved a similar performance level, with only an average score of 1.2.

Delving into the detailed distribution of scores for responses generated by BiomedGPT and GPT-4V, we noticed that BiomedGPT predominantly produced 'correct' answers, as depicted in **Fig. 6c**. For instance, in the categories of presence and type questions, BiomedGPT accurately answered 100% of the queries. In other categories, except for view-related questions, BiomedGPT managed to answer all questions either correctly or partially correctly. On the other hand, GPT-4V's performance was not as robust, particularly when compared to its previous zero-shot learning performance on VQA-RAD (**Fig. 5c-d**). GPT-4V either answered incorrectly or provided unrelated responses to 16 out of the 52 questions. One possible explanation for this discrepancy is that BiomedGPT has been fine-tuned with relevant training data, enabling better alignment of answers with questions. Conversely, GPT-4V does not offer fine-tuning capabilities, and institutions often hesitate to upload data over the internet due to privacy concerns. Another contributing factor could be the dataset used for our human evaluation. This dataset, derived from MIMIC-CXR as of September 15, 2023, had never been used to train GPT-4V, possibly leading to its lower performance in our tests.

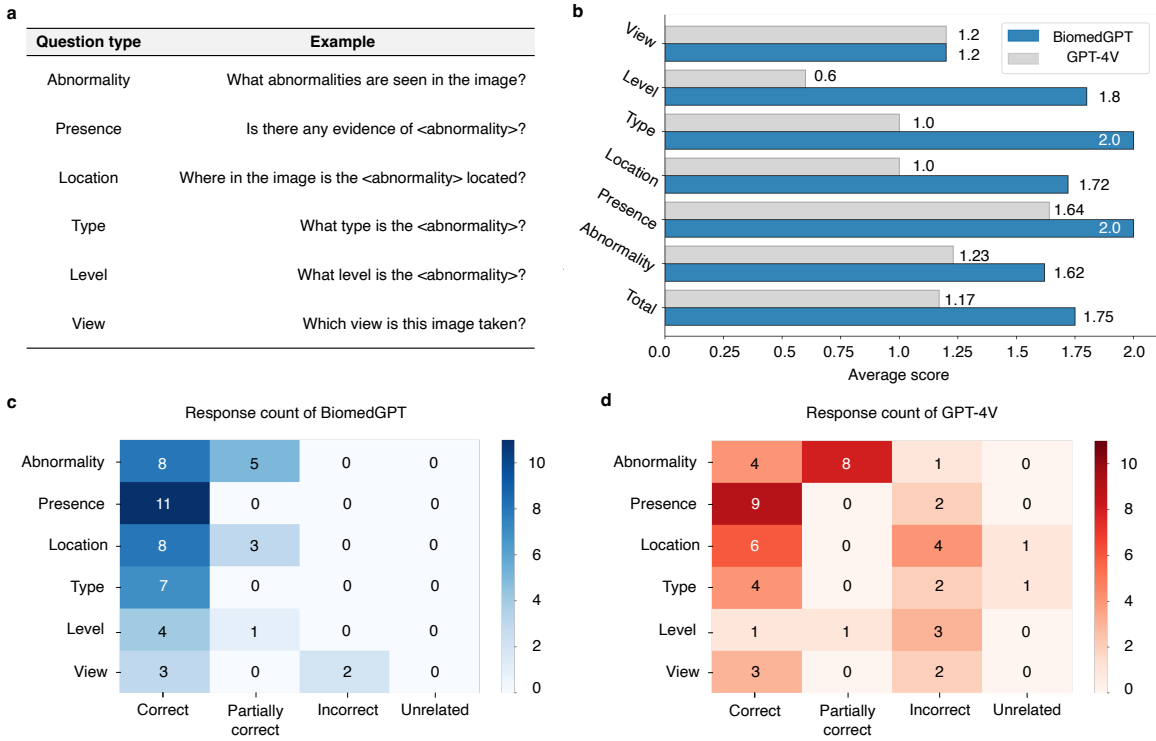


Figure 6: Human evaluation on the VQA task. **(a)** Description of question types and examples used for human evaluation. **(b)** Human rating in terms of the question type. Here we compared GPT-4V and BiomedGPT. **(c)** Details of the quality evaluation of the generated answers from BiomedGPT. **(d)** Details of the quality evaluation of the generated answers from GPT-4V.

Conducting extensive human evaluation presents challenges for us, primarily due to the limited availability of professional medical practitioners. This scarcity makes it difficult to scale up such evaluations. Moreover, in our interactions with GPT-4V, we noted its tendency to initially reject answering clinical questions, necessitating multiple rounds of conversation to coax out responses. This pattern highlights GPT-4V’s sensitivity to conversational prompts and its reliance on extended dialogues, which can sometimes lead to varying answers. This aspect and related findings are also discussed in the official system card of GPT-4V [35]. Given these factors, our evaluation should be considered more as a case study rather than a comprehensive assessment. Nevertheless, it offers a glimpse into BiomedGPT’s potential for deployment in biomedical settings. Particularly notable is BiomedGPT’s ease of use, which could make it a valuable tool in medical institutions. This attribute, combined with the promising results from our study, underscores BiomedGPT’s potential as a practical and accessible solution in the field of biomedical artificial intelligence.

3 Discussion

In this study, we have shown that BiomedGPT can achieve competitive transfer learning performance across various tasks, across vision, language, and multimodal domains. This is achieved by integrating a diverse range of biomedical modalities and tasks within a unified seq2seq pretraining framework. In our pioneering research focused on a generalist biomedical AI system, we have carried out a comprehensive array of experiments, trials, and in-depth analyses. In this section, we delve into the limitations and areas for potential enhancement of our study. These insights are drawn not only from the findings detailed in the **Results** section but also from additional demonstration experiments provided as supplementary material.

The development of a unified biomedical AI is primarily constrained by the availability of large-scale and diverse high-quality data. The development of general-purpose models has been critically dependent on the availability of high-quality, annotated data [91]. This requirement poses a unique challenge in the biomedical domain, where data annotation is not only expensive and time-consuming but also demands extensive domain expertise and years of specialized education [77, 92]. Consequently, AI researchers often resort to public datasets, which, however, present several concerns regarding data quality: (1) **Imbalance in domain diversity.** Public biomedical datasets predominantly focus on radiology, with chest X-ray data being the most abundant. Other anatomical areas and imaging modalities are relatively underrepresented. Pathology, especially surgical pathology and microscopic images, forms another major category. However, compared to radiology and pathology, datasets covering areas like retinal fundus and dermatoses are considerably scarce. This imbalance in domain representation posed significant challenges in our study, making it difficult to achieve a balance in pretraining data across different fields. When dealing with multimodal biomedical datasets, particularly image-text pairs, the imbalance becomes even more pronounced. To the best of our knowledge, almost all existing datasets for VQA and image captioning are centered around radiology. (2) **Scarcity of large-scale multimodal biomedical data.** In contrast to the abundance of vision-only datasets, which include unlabeled or weakly-labeled biomedical images, and the plentiful supply of language-only data such as biomedical articles from PubMed or PMC, the quantity of extensive vision-language biomedical datasets is significantly limited. This scarcity poses a substantial challenge to the development of generalist biomedical AI models, specifically, hampers the ability of these models to learn comprehensive representations that span across both visual and textual biomedical information. While utilizing advanced general-purpose models like GPT-4V to label or caption images might seem a viable solution to augment image-text pairs, it raises concerns about the reliability of such weakly-labeled or captioned texts that could potentially introduce biases or inaccuracies.

There is no perfect automatic evaluation manner for generative biomedical tasks. In our study, we implemented a Trie-based search strategy, as detailed in the **Methods** section, to ensure that BiomedGPT's answers remain within a predefined set of candidates. This approach helps avoid generating freeform responses, which present significant challenges for automatic evaluation in terms of correctness and factual accuracy. However, for broader applications of BiomedGPT, such as in zero-shot learning scenarios where no candidate set is provided, we anticipate the model to generate correct answers in a freeform manner to any given question. In these cases, automatic evaluation becomes more complex, and manual review of the generated responses may be necessary to ensure their accuracy and relevance. Evaluating the quality of generated image captions and text summarizations presents significant challenges. While metrics like CIDEr and ROUGE-L can gauge the consensus between generated content and the gold standard, ensuring the factual accuracy of these outputs remains a concern. To address this, recent research introduced the F1-RadGraph score [93]. This metric utilizes the RadGraph dataset [94], which contains annotated chest X-ray reports with identified entities and their relationships, to qualitatively assess the factual correctness and completeness of generated reports. In other domains like pathology, however, similar evaluation metrics are not yet prevalent. Drawing inspiration from factual-concerned metrics developed in radiology [95, 93], we anticipate the emergence of analogous metrics for these domains. These would further enhance our ability to measure the factual integrity and overall quality of AI-generated medical content across various biomedical fields.

Expanding BiomedGPT with more modalities and tasks is feasible but how to tackle the negative transfer needs further exploration. BiomedGPT, currently adept in processing images and texts, could

potentially extend its capabilities to other types of biomedical data, such as tabular [79], video [96], 3D images[97], and time-series/sequential data [98]. Inspired by studies implementing transformer architectures for these data types [99, 100, 101], BiomedGPT can be adapted to handle a wider array of data formats. Nevertheless, this expansion raises concerns about negative transfer, where learning from additional modalities might inadvertently hamper performance on certain tasks. For instance, our ablation study revealed that excluding image data during pretraining improves performance on language-only downstream tasks (Fig. 4b), highlighting the risk of negative transfer. Incorporating more modalities and tasks increases the disparity in pretraining data, which might adversely affect unimodal or unrelated downstream tasks. To mitigate this, we propose exploring controllable or editable transfer learning strategies. One approach is the Mixture of Experts (MoE) model [102], which employs gating networks to determine the most suitable 'experts' (specific sets of model parameters) based on the input data modalities. Another strategy involves identifying and modifying key neuron activations that underpin factual predictions in a model [103]. Specifically, mid-layer feed-forward modules in transformers store factual associations, and by adjusting certain model weights, we can update these factual associations to better suit specific downstream tasks. Such approaches could be potential to offer more tailored and effective training, harnessing the full potential of multi-modal data without the drawbacks of negative transfer.

Potential for performance enhancement through model scaling in BiomedGPT. Evidence from our comprehensive analysis (Fig. 2b-c, Fig. 3d-f, Fig. 4e-f, and Fig. 5d) indicates a direct correlation between increased model scale and enhanced performance, applicable to both zero-shot predictions and post-fine-tuning. While our current efforts were constrained by storage and computational resources, preventing further scaling of BiomedGPT, we encourage others to leverage our open-source code to explore this potential. Scaling up the model could yield substantial performance gains. However, scaling brings its own set of challenges, particularly concerning fine-tuning efficiency, training speed, and memory requirements. This is especially pertinent when developing large-scale generalist biomedical models. To address these challenges, an intriguing area of research is parameter-efficient fine-tuning (PEFT) [104, 105, 106]. PEFT strategies involve fine-tuning a minimal subset of model parameters while keeping the majority of pre-trained parameters static. In our experiments, we experimented with prompt tuning [107], but it did not yield the anticipated outcomes (Extended Fig. 3). Recent advancements like LoRA [108, 109] have demonstrated improved results compared to earlier PEFT methods, indicating a promising direction for future enhancements to BiomedGPT.

Enhancing text understanding and multi-inputs processing are expected. Our zero-shot transfer learning tests (Fig. 5c) revealed that BiomedGPT's text comprehension capabilities, especially in comparison with GPT-4V, are not fully established. Typically, robust text understanding stems from large-scale language models. In our case, two primary factors limit this capability: first, the current scale of BiomedGPT, which, although expandable, is constrained by available resources; second, the use of a single decoder designed to process various input types, not exclusively text. This architecture might introduce noise and lead to negative interferences between different data types. Contemporary unified biomedical AI models like LLaVa-Med [28] and Med-PaLM M have integrated pre-trained large language models, aligning visual features through a trainable projection matrix. This approach, however, necessitates fine-tuning the entire large language model, an expensive endeavor given their substantial size. Moreover, a critical gap in current multimodal biomedical AI models, including BiomedGPT, is their inability to process multiple inputs simultaneously, particularly multiple images – a common requirement in clinical settings where practitioners may need to analyze several CT scans concurrently. Even general-purpose systems like GPT-4V, which can handle up to four images, fall short in addressing the needs of real-world biomedical and healthcare applications. Addressing this limitation is a pivotal goal for our next phase of development, aiming to make BiomedGPT a more versatile tool in practical scenarios.

4 Methods

Our proposed BiomedGPT is a transformer-based architecture specifically designed for the biomedical field, built upon the success of existing unified models for general data. We follow the fundamental principles of a unified model: 1) Modality-Agnostic, 2) Task-Agnostic, and 3) Modality and Task Comprehensiveness. By discretizing data into patches or tokens, we achieve input/output unification using ideas from ViT [110] and language models [111]. We pre-trained our model on a diverse set of biomedical modalities and tasks to enhance its transferability. Our encoder-decoder architecture maps multi-modal data with task-related instructions into a common representation space, which helps to address discrepancies among biomedical modalities.

4.1 Description of the BiomedGPT architecture

We follow OFA [33] to design BiomedGPT, which takes BART [70] as the backbone that is implemented as a sequence-to-sequence model with a BERT-style encoder over corrupted text and a GPT-style left-to-right autoregressive decoder. All of these models rely on transformer with multi-head attention mechanism (**Extended Fig. 1a**) that is popularly used which allows the model to jointly attend to the information from different representation sub-spaces [112]. A few architectural changes are made to adapt the BART architecture for BiomedGPT. First, to improve the convergence efficiency and stability in the pretraining, we add three normalization operations to each layer: a post-attention Layer Norm (LN) [113], post-first-FFN LN, and head-wise scaling within self-attention (**Fig. 7d and Extended Fig. 1a**), following [114]. To encode positional information, we incorporate two sets of absolute position embeddings for both text and images. Rather than merely combining these embeddings with token and patch embeddings, we implement a decoupling method to separate position correlation (**Extended Fig. 1b**), which may bring unnecessary randomness in the attention and further limit the expressiveness of the model [115, 112]. Furthermore, we also incorporate 1D relative position bias for text and 2D relative position bias for image (**Extended Fig. 1c**), as described in previous works [69, 116, 117]. In order to investigate the performance of BiomedGPT for tasks at different scales, we explicitly design three scaling models, i.e., BiomedGPT-S (33M), BiomedGPT-M (93M), and BiomedGPT-B (182M). The configurations for each model are detailed in **Extended Table. 4**.

4.2 Input/output unification

To handle diverse modalities without relying on task-specific output structures, we represent them with tokens drawn from a unified and finite vocabulary (**Fig. 7b**). To achieve this, we utilize the frozen image quantization [118, 119] and object descriptor [120, 121] to discretize the images and objects on the target side, respectively. As to the text outputs, such as object labels and summarizations, we represent them with BPE tokens. To be more specific, the image with 256×256 resolution is sparsely encoded into a sequence of 16×16 , which is strongly correlated with the corresponding patch [122] and can effectively reduce the sequence length of the image representation. The bounding boxes of objects in an image are expressed as sequences of location tokens in the format of integers. We hereby build a unified vocabulary for all tokens of multi-modal outputs. The total vocabulary size is 59457, with 50265 language tokens, 1000 location tokens, and 8192 vision tokens. The number of vision tokens is determined by the variant of the pre-trained VQ-GAN models used in the BiomedGPT, specifically, the OpenImages[123]-trained VQ-GAN with patch size of 8 and vocabulary size of 8192 using the Gumbel softmax [124, 125] quantization. During training, we randomly subsample 196 image patches for pretraining. The truncation to max model input length is set as 512.

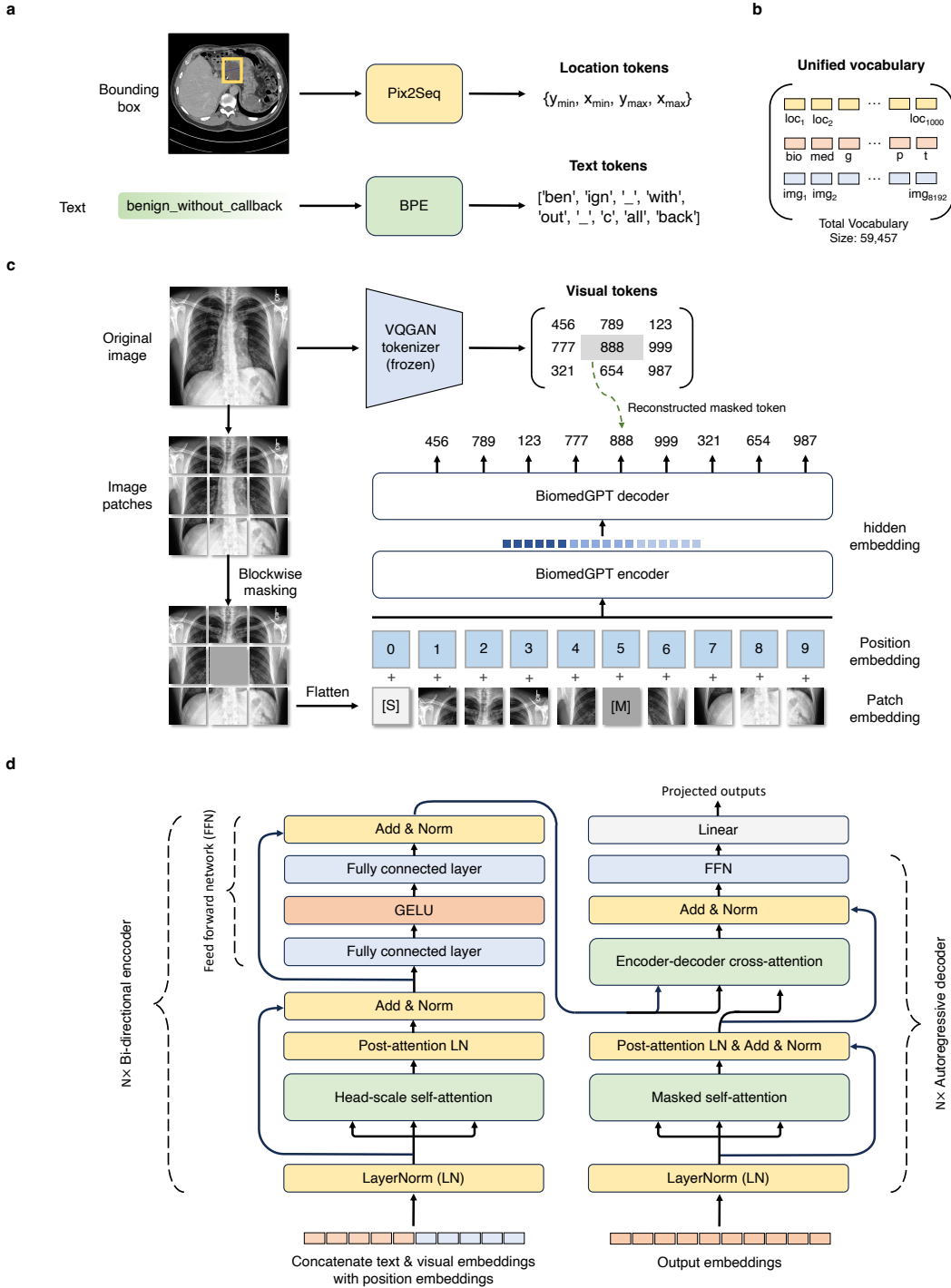


Figure 7: Graphical demonstration of BiomedGPT’s design. **(a)** Tokenization of bounding box and text via Pix2Seq and BPE, respectively. **(b)** Description of the unified vocabulary used in BiomedGPT for pretraining and inference. There are three types of the token: location tokens, text tokens and image tokens from the frozen pre-trained tokenizers such as VQGAN. **(c)** Graphical illustration of masked image modeling in the pretraining, which aims to learn the representations via reconstructing the masked patches. **(d)** The neural network architecture of BiomedGPT, which includes bi-directional encoder blocks and autoregressive decoder blocks. The number of blocks vary for different model scales.

4.3 Natural language as a task manager

Multitasking is a key attribute of a unified and generalist model. Following previous literature on language models using prompt / instruction learning [32, 40, 41, 42, 43], and the existing unified frameworks to eliminate task-specific modules, we specify each task with a handcrafted instruction excluding like (Fig. 2a), which are fully specified by their text inputs. BiomedGPT supports abstractions of several tasks, including vision-only, text-only, and vision-language, to achieve task comprehensiveness. We provide details of the pretraining tasks, fine-tuning / inference tasks, as well as their corresponding instructions in the following.

Pretraining tasks. We consider two vision-only tasks in the pretraining: for masked image modeling as well as image infilling, we borrow the idea of blockwise masking [126] and let the model recover the masked patches in the middle part by generating the corresponding codes (see Fig. 7c). The corresponding instruction is “*What is the image in the middle part?*”. For object detection, the model learns to generate the bounding box of an object with the instruction of “*What are the objects in the image?*”. As to the text-only task, we adopt the commonly-used masked language modeling, whose logic is similar to the masked image modeling, while the instruction is “*What is the complete text of ‘{Text}’ ?*” (Fig. 4a). Two types of multi-modal tasks are selected, including image captioning with the instruction of “*What does the image describe?*” and VQA with the instruction of “*{Question}*”. The addition of object detection for pretraining BiomedGPT serves to enhance visual learning inspired by [127].

Fine-tuning and downstream tasks. Besides image captioning and VQA used in pretraining, we cover one more vision-only task and two more text-only tasks. Specifically, we use the instruction “*What does the image describe?*” to differentiate image classification. “*What is the summary of text ‘{Text}’?*” and “*Can text1 ‘{Text1}’ imply text2 ‘{Text2}’?*” are exploited for text summarization and natural language inference, respectively.

4.4 Autoregressive generative training and tuning

All experiments were run in Python v.3.7.4. Detailed software versions are: pytorch v.1.8.1; CUDA v.12.2; fairseq v.1.0.0; torchvision v.0.9.1; numpy v.1.21.5; pandas v.1.3.5; PIL v.9.0.1; timm v.0.6.12; opencv-python v.4.6.0; pycocotools v.2.0.4; pycocoevalcap v.1.2; einops v.0.6.0; ftfy v.6.0.3; torchmetrics v.0.11.0.

Model training. We adopted autoregressive or sequence-to-sequence (seq2seq) learning [128, 129, 130], which is the commonly-used approach for large language models [70, 69], to train our BiomedGPT. Formally, suppose we are given a sequence of tokens $\mathbf{x}_{i,b}$ as input, where $i = 1, \dots, I$ indexes the tokens in a data sample and $b = 1, \dots, B$ indexes a sample in a training batch. Let a model be parametrized by θ . Then we autoregressively train the model by minimizing:

$$\mathcal{L}_{\theta}(\mathbf{x}_{1,1}, \dots, \mathbf{x}_{i,b}) = - \sum_{b=1}^B \log \prod_{i=1}^I p_{\theta}(\mathbf{x}_{i,b} | \mathbf{x}_{1,b}, \dots, \mathbf{x}_{i-1,b}) = - \sum_{b=1}^B \sum_{i=1}^I \log p_{\theta}(\mathbf{x}_{i,b} | \mathbf{x}_{<i,b})$$

In the context of BiomedGPT, \mathbf{x} could refer to both linguistic and visual tokens in the pretraining tasks, including subwords, image codes, and location tokens. Specifically, subwords are extracted by a BPE tokenizer, and we mask 15% of the tokens of the subwords in input in the masked language modeling task as these medical words show relatively high overlapping degrees. For the object detection task, location tokens are generated with Pix2Seq [120] conditioned on the observed pixel inputs. We need data preprocessing for quantizing biomedical images using VQ-GAN [119] because they are surrounded by trivial semantics, e.g., black background and the unmet input size. Therefore, we first remove the trivial background and crop the image to the bounding box of the object of interest, then resize the cropped image to be 256×256 , and feed the center part with 128×128 resolution into the pre-trained VQ-GAN to generate the corresponding sparse image codes, which are the target output in masked image modeling

task. Vision-language tasks follow the same tokenization flow. Note that for fine-tuning, we also apply seq2seq learning but with different datasets and tasks.

To pretrain our BiomedGPT, we use the AdamW [131] optimizer with hyperparameters $\beta_1 = 0.9$, $\beta_2 = 0.999$, and $\epsilon = 1e-8$. The peak learning rate is set to $1e-4$, and we apply a linear decay scheduler with a warmup ratio of 0.01 to control the learning rate. For regularization, we set dropout to 0.1 and use a weight decay of 0.01. To enhance the training process, we use stochastic depth with a rate of 0.1 applied to the encoder and decoder, except for convolution blocks. Furthermore, we employ a diversified approach in mixing all pretraining data within each batch. This includes an assortment of multi-modal, text-only, vision-only, and object detection samples. The ratio applied is 8:2:1:1, which emphasizes learning and enhancing the interaction between vision and language. The models are pre-trained with 10 NVIDIA A5000 GPUs and mixed precision [132].

Model tuning and efficient inference. Fine-tuning, a form of transfer learning, involves adapting a pre-trained model’s weights to new data. The practice of fine-tuning pre-trained models, a widely acknowledged and highly effective approach in natural language processing and computer vision, has also found significant application in medical AI [133, 134]. Different from most previous biomedical models that necessitate the addition and training of extra components, such as a linear output layer or a decoder, our BiomedGPT model solely relies on fine-tuning the existing structure. The specific instructions employed for this fine-tuning procedure mirror the pretraining workflow, thereby maintaining consistency and efficiency in model adaptation.

Similar to the existing large language models or multimodal models [33], in inference, we used the decoding strategies such as beam search to improve generation quality. However, such an approach poses challenges for classification tasks, including unnecessary search of the entire vocabulary and the possibility of generating invalid labels beyond the closed label set. To tackle these issues, we apply a beam search strategy that incorporates a prefix tree (also known as a trie), limiting the number of candidate tokens and resulting in more efficient and accurate decoding. **Extended Fig. 1d** demonstrates an example of trie-based beam search; along the path across “Lipid” and “breakdown”, BiomedGPT sets logits for all invalid tokens (“mechanism” and “pathway”) to $-\infty$ when computing log-probabilities for the target token “in”. It is worth noting that trie-based search is also applied during the validation phase of the fine-tuning stage for acceleration (approximately $16\times$ increase in speed in our experiments).

4.5 Evaluation metrics

In this paper, we employ various evaluation metrics to thoroughly assess the capabilities of our BiomedGPT model across different tasks. Accuracy is a primary metric used for evaluating the performance in medical image classification, VQA and natural language inference. In addition to accuracy, we also utilize the F1 score for these tasks considering class imbalance, where the F1 score is derived as the harmonic mean of precision and recall:

$$F1 = \frac{2 \times \text{precision} \times \text{recall}}{\text{precision} + \text{recall}} \quad (1)$$

Specifically, for a more convenient comparison with state-of-the-art approaches, we use the weighted F1 score for VQA. This measure is computed by averaging the F1 scores across each class, with the individual class scores weighted according to their frequency of occurrence:

$$F1\text{-Weighted} = \sum_{i=1}^N \frac{n_i}{N} \times F1_i, \quad (2)$$

where n_i is the number of instances in class i , N is the total number of instances across all classes, and $F1_i$ is the F1 score for class i .

Furthermore, we apply the macro-average F1 score (F1-Macro) in image classification tasks on the CBIS-DDSM dataset. The F1-Macro score is calculated by determining the F1 score for each class independently and then averaging these scores across all classes. This approach does not account for class imbalances, treating each class with equal importance:

$$\text{F1-Macro} = \frac{1}{N} \times \sum_{i=1}^N \text{F1}_i \quad (3)$$

The higher accuracy and F1 score (either weighted- or macro-average), the better performance the model achieves.

ROUGEL-L was used to evaluate the quality of the generated text on the tasks of image captioning and text summarization, which stands for recall-oriented understudy for gisting evaluation with the longest common subsequence. Given the candidate C and reference R , let $LCS(C, R)$ be the length of the longest common subsequence, which is determined by using dynamic programming, it can be an expression as:

$$\text{ROUGE-L} = \frac{(1 + \beta^2)R_{LCS}P_{LCS}}{R_{LCS} + \beta^2P_{LCS}}, \quad (4)$$

where $R_{LCS} = \frac{LCS(C,R)}{c}$, $P_{LCS} = \frac{LCS(C,R)}{r}$, $\beta = \frac{P_{LCS}}{R_{LCS}}$. c and r represent the length of the candidate and reference. A higher ROUGE-L score means that the generated text shares more of the same sequences of words as the reference text, which typically indicates better quality in terms of capturing the salient points of the reference. It suggests that the generated text is more similar to the reference summaries that it is being compared to, which is usually desired in summarization tasks.

In addition to ROUGEL-L, we also applied METEOR and CIDEr to get a more comprehensive evaluation of captioning generation quality. In details, METEOR stands for metric for evaluation of translation with explicit ordering. We represent precision and recall as $P = \frac{m}{c}$ and $R = \frac{m}{r}$ and let m be the number of common words in the candidate C and the reference R with the number of words of c and r , respectively. The METEOR is calculated via:

$$\text{METEOR} = (1 - p) \times \frac{PR}{\alpha P + (1 - \alpha)R} \quad (5)$$

where p is the penalty factor and is denoted as $p = \gamma(\frac{ch}{m})^\theta$, ch is the number of chunks, which means a contiguous ordered block. α, θ, γ are hyperparameters determined according to different datasets.

CIDEr is specifically designed to evaluate the quality of captions of images, which stands for consensus-based image description evaluation. The CIDEr score is calculated based on n-gram matching, considering both precision (how many n-grams in the generated caption are also in the reference captions) and recall (how many n-grams in the reference captions are also in the generated caption). It also weights the n-grams based on their saliency (importance in describing the image) and rarity (uncommonness in the dataset), which helps to emphasize the importance of capturing the most relevant aspects of the image in the caption. Let c be a candidate caption, S be a set of reference captions, and CIDEr is obtained by averaging the similarity of different lengths:

$$\text{CIDEr}_n(c, S) = \frac{1}{M} \sum_{i=1}^M \frac{g^n(c) \times g^n(S_i)}{\|g^n(c)\| \times \|g^n(S_i)\|}, \quad (6)$$

where M denotes the number of reference captions and $g^n(\cdot)$ denotes an n -gram-based TF-IDF vector. A higher CIDEr score suggests that the generated caption is more accurate and descriptive of the image content, aligning well with human judgments of what the image represents. CIDEr can technically range from 0 to 100. Typically, human captions would tend to score near 90.

5 Data Availability

All data in this study is publicly available and can be accessed from: VQA-RAD (<https://osf.io/89kps/>), SLAKE 1.0 (<https://www.med-vqa.com/slake/>), PathVQA (<https://github.com/UCSD-AI4H/PathVQA>), IU-XRAY and PEIR GROSS (<https://github.com/nlpaueb/bioCaption>), MediCat (<https://github.com/allenai/medicat>), MedMNIST v2 (<https://medmnist.com>), SZ-CXR and MC-CXR can be requested via the contact on (<http://archive.nlm.nih.gov/repos/chestImages.php>), CBIS-DDSM (<https://www.kaggle.com/datasets/awsaf49/cbis-ddsm-breast-cancer-image-dataset>), CheXpert-v1.0-small (<https://www.kaggle.com/datasets/willarevalo/chexpert-v10-small>), CytolImageNet (<https://www.kaggle.com/datasets/stanleyhua/cytoimagenet>), MIMIC-CXR (<https://physionet.org/content/mimic-cxr-jpg/2.0.0/>), MIMIC-III (<https://physionet.org/content/mimiciii/1.4/>), HealthcareMagic (<https://github.com/UCSD-AI4H/Medical-Dialogue-System>), MeQSum (<https://huggingface.co/datasets/sumedh/MeQSum>), MedNLI (<https://physionet.org/content/mednli/1.0.0/>), PubMed Abstracts are derived from BLUE benchmark (https://github.com/ncbi-nlp/BLUE_Benchmark), NCBI BioNLP (<https://www.ncbi.nlm.nih.gov/research/bionlp/Data/>), ROCO (<https://github.com/razorx89/roco-dataset>), DeepLesion (<https://nihcc.app.box.com/v/DeepLesion>), ISIC 2020 (<https://challenge2020.isic-archive.com>), Retinal Fundus (<https://www.kaggle.com/c/diabetic-retinopathy-detection>). The data for human evaluation are derived from Medical-Diff-VQA (<https://physionet.org/content/medical-diff-vqa/1.0.0/>), with the exclusion of questions related to differences, as these require a two-image input; the IDs of patient and study with the corresponding questions for rating were provided in the supplementary material.

6 Code Availability

The pre-trained and fine-tuned models as well as source codes for training, inference and data preprocessing can be accessed at <https://github.com/taokz/BiomedGPT>.

References

- [1] A. Vaswani, N. Shazeer, N. Parmar, J. Uszkoreit, L. Jones, A. N. Gomez, Ł. Kaiser, and I. Polosukhin, "Attention is all you need," *Advances in neural information processing systems*, vol. 30, 2017.
- [2] C. Zhou, Q. Li, C. Li, J. Yu, Y. Liu, G. Wang, K. Zhang, C. Ji, Q. Yan, L. He *et al.*, "A comprehensive survey on pretrained foundation models: A history from bert to chatgpt," *arXiv preprint arXiv:2302.09419*, 2023.
- [3] M. Wornow, Y. Xu, R. Thapa, B. Patel, E. Steinberg, S. Fleming, M. A. Pfeffer, J. Fries, and N. H. Shah, "The shaky foundations of large language models and foundation models for electronic health records," *npj Digital Medicine*, vol. 6, no. 1, p. 135, 2023.
- [4] A. J. Thirunavukarasu, D. S. J. Ting, K. Elangovan, L. Gutierrez, T. F. Tan, and D. S. W. Ting, "Large language models in medicine," *Nature medicine*, pp. 1–11, 2023.
- [5] A. Kline, H. Wang, Y. Li, S. Dennis, M. Hutch, Z. Xu, F. Wang, F. Cheng, and Y. Luo, "Multimodal machine learning in precision health: A scoping review," *npj Digital Medicine*, vol. 5, no. 1, p. 171, 2022.
- [6] Z. Liu, A. Zhong, Y. Li, L. Yang, C. Ju, Z. Wu, C. Ma, P. Shu, C. Chen, S. Kim *et al.*, "Radiology-gpt: A large language model for radiology," *arXiv preprint arXiv:2306.08666*, 2023.
- [7] C. Liu, Z. Liu, J. Holmes, L. Zhang, L. Zhang, Y. Ding, P. Shu, Z. Wu, H. Dai, Y. Li *et al.*, "Artificial general intelligence for radiation oncology," *arXiv preprint arXiv:2309.02590*, 2023.
- [8] R. Luo, L. Sun, Y. Xia, T. Qin, S. Zhang, H. Poon, and T.-Y. Liu, "Biogpt: generative pre-trained transformer for biomedical text generation and mining," *Briefings in Bioinformatics*, vol. 23, no. 6, p. bbac409, 2022.
- [9] D. Van Veen, C. Van Uden, M. Attias, A. Pareek, C. Bluethgen, M. Polacin, W. Chiu, J.-B. Delbrouck, J. Zambrano Chaves, C. Langlotz, A. Chaudhari, and J. Pauly, "RadAdapt: Radiology report summarization via lightweight domain adaptation of large language models," in *The 22nd Workshop on Biomedical Natural Language Processing and BioNLP Shared Tasks*. Association for Computational Linguistics, 2023, pp. 449–460.
- [10] L. Rasmy, Y. Xiang, Z. Xie, C. Tao, and D. Zhi, "Med-bert: pretrained contextualized embeddings on large-scale structured electronic health records for disease prediction," *NPJ digital medicine*, vol. 4, no. 1, p. 86, 2021.
- [11] Y. Zhou, M. A. Chia, S. K. Wagner, M. S. Ayhan, D. J. Williamson, R. R. Struyven, T. Liu, M. Xu, M. G. Lozano, P. Woodward-Court *et al.*, "A foundation model for generalizable disease detection from retinal images," *Nature*, pp. 1–8, 2023.
- [12] J.-b. Delbrouck, K. Saab, M. Varma, S. Eyuboglu, P. Chambon, J. Dunnmon, J. Zambrano, A. Chaudhari, and C. Langlotz, "Vilmedic: a framework for research at the intersection of vision and language in medical ai," in *Proceedings of the 60th Annual Meeting of the Association for Computational Linguistics: System Demonstrations*, 2022, pp. 23–34.
- [13] M. E. Tinetti, A. D. Naik, L. Dindo, D. M. Costello, J. Esterson, M. Geda, J. Rosen, K. Hernandez-Bigos, C. D. Smith, G. M. Ouellet *et al.*, "Association of patient priorities–aligned decision-making with patient outcomes and ambulatory health care burden among older adults with multiple chronic conditions: a nonrandomized clinical trial," *JAMA internal medicine*, vol. 179, no. 12, pp. 1688–1697, 2019.
- [14] R. Jayadevappa and S. Chhatre, "Patient centered care-a conceptual model and review of the state of the art," *The Open Health Services and Policy Journal*, vol. 4, no. 1, 2011.
- [15] M. K. Constand, J. C. MacDermid, V. Dal Bello-Haas, and M. Law, "Scoping review of patient-centered care approaches in healthcare," *BMC health services research*, vol. 14, pp. 1–9, 2014.

- [16] A. D. Naik, L. N. Dindo, J. R. Van Liew, N. E. Hundt, L. Vo, K. Hernandez-Bigos, J. Esterson, M. Geda, J. Rosen, C. S. Blaum *et al.*, “Development of a clinically feasible process for identifying individual health priorities,” *Journal of the American Geriatrics Society*, vol. 66, no. 10, pp. 1872–1879, 2018.
- [17] M. Moor, O. Banerjee, Z. S. H. Abad, H. M. Krumholz, J. Leskovec, E. J. Topol, and P. Rajpurkar, “Foundation models for generalist medical artificial intelligence,” *Nature*, vol. 616, no. 7956, pp. 259–265, 2023.
- [18] J. N. Acosta, G. J. Falcone, P. Rajpurkar, and E. J. Topol, “Multimodal biomedical ai,” *Nature Medicine*, vol. 28, no. 9, pp. 1773–1784, 2022.
- [19] S. Reed, K. Zolna, E. Parisotto, S. G. Colmenarejo, A. Novikov, G. Barth-marion, M. Giménez, Y. Sulsky, J. Kay, J. T. Springenberg, T. Eccles, J. Bruce, A. Razavi, A. Edwards, N. Heess, Y. Chen, R. Hadsell, O. Vinyals, M. Bordbar, and N. de Freitas, “A generalist agent,” *Transactions on Machine Learning Research*, 2022, featured Certification, Outstanding Certification. [Online]. Available: <https://openreview.net/forum?id=1kkK0kHvj>
- [20] J. Lu, C. Clark, R. Zellers, R. Mottaghi, and A. Kembhavi, “UNIFIED-IO: A unified model for vision, language, and multi-modal tasks,” in *The Eleventh International Conference on Learning Representations*, 2023. [Online]. Available: <https://openreview.net/forum?id=E01k9048soZ>
- [21] T. Tu, S. Azizi, D. Driess, M. Schaeckermann, M. Amin, P.-C. Chang, A. Carroll, C. Lau, R. Tanno, I. Ktena *et al.*, “Towards generalist biomedical ai,” *arXiv preprint arXiv:2307.14334*, 2023.
- [22] A. Chowdhery, S. Narang, J. Devlin, M. Bosma, G. Mishra, A. Roberts, P. Barham, H. W. Chung, C. Sutton, S. Gehrmann *et al.*, “Palm: Scaling language modeling with pathways,” *arXiv preprint arXiv:2204.02311*, 2022.
- [23] A. Dosovitskiy, L. Beyer, A. Kolesnikov, D. Weissenborn, X. Zhai, T. Unterthiner, M. Dehghani, M. Minderer, G. Heigold, S. Gelly, J. Uszkoreit, and N. Houlsby, “An image is worth 16x16 words: Transformers for image recognition at scale,” in *International Conference on Learning Representations*, 2021. [Online]. Available: <https://openreview.net/forum?id=YicbFdNTTy>
- [24] D. Driess, F. Xia, M. S. Sajjadi, C. Lynch, A. Chowdhery, B. Ichter, A. Wahid, J. Tompson, Q. Vuong, T. Yu *et al.*, “Palm-e: An embodied multimodal language model,” *arXiv preprint arXiv:2303.03378*, 2023.
- [25] A. Radford, J. W. Kim, C. Hallacy, A. Ramesh, G. Goh, S. Agarwal, G. Sastry, A. Askell, P. Mishkin, J. Clark *et al.*, “Learning transferable visual models from natural language supervision,” in *International conference on machine learning*. PMLR, 2021, pp. 8748–8763.
- [26] H. Touvron, T. Lavril, G. Izacard, X. Martinet, M.-A. Lachaux, T. Lacroix, B. Rozière, N. Goyal, E. Hambro, F. Azhar *et al.*, “Llama: Open and efficient foundation language models,” *arXiv preprint arXiv:2302.13971*, 2023.
- [27] Z. Chen, Y. Du, J. Hu, Y. Liu, G. Li, X. Wan, and T.-H. Chang, “Multi-modal masked autoencoders for medical vision-and-language pre-training,” in *International Conference on Medical Image Computing and Computer-Assisted Intervention*. Springer, 2022, pp. 679–689.
- [28] C. Li, C. Wong, S. Zhang, N. Usuyama, H. Liu, J. Yang, T. Naumann, H. Poon, and J. Gao, “Llava-med: Training a large language-and-vision assistant for biomedicine in one day,” *arXiv preprint arXiv:2306.00890*, 2023.
- [29] J. D. M.-W. C. Kenton and L. K. Toutanova, “Bert: Pre-training of deep bidirectional transformers for language understanding,” in *Proceedings of NAACL-HLT*, 2019, pp. 4171–4186.
- [30] A. Radford, K. Narasimhan, T. Salimans, I. Sutskever *et al.*, “Improving language understanding by generative pre-training,” *OpenAI blog*, 2018.
- [31] A. Radford, J. Wu, R. Child, D. Luan, D. Amodei, I. Sutskever *et al.*, “Language models are unsupervised multitask learners,” *OpenAI blog*, vol. 1, no. 8, p. 9, 2019.

- [32] T. Brown, B. Mann, N. Ryder, M. Subbiah, J. D. Kaplan, P. Dhariwal, A. Neelakantan, P. Shyam, G. Sastry, A. Askell *et al.*, “Language models are few-shot learners,” *Advances in neural information processing systems*, vol. 33, pp. 1877–1901, 2020.
- [33] P. Wang, A. Yang, R. Men, J. Lin, S. Bai, Z. Li, J. Ma, C. Zhou, J. Zhou, and H. Yang, “Ofa: Unifying architectures, tasks, and modalities through a simple sequence-to-sequence learning framework,” in *International Conference on Machine Learning*. PMLR, 2022, pp. 23 318–23 340.
- [34] X. Tang, J. Zhang, Y. He, X. Zhang, Z. Lin, S. Partarrieu, E. B. Hanna, Z. Ren, H. Shen, Y. Yang *et al.*, “Explainable multi-task learning for multi-modality biological data analysis,” *Nature Communications*, vol. 14, no. 1, p. 2546, 2023.
- [35] OpenAI, “Gpt-4v(ision) system card,” https://cdn.openai.com/papers/GPTV_System_Card.pdf, 2023.
- [36] R. Balestriero, M. Ibrahim, V. Sobal, A. Morcos, S. Shekhar, T. Goldstein, F. Bordes, A. Bardes, G. Mialon, Y. Tian *et al.*, “A cookbook of self-supervised learning,” *arXiv preprint arXiv:2304.12210*, 2023.
- [37] S.-C. Huang, A. Pareek, M. Jensen, M. P. Lungren, S. Yeung, and A. S. Chaudhari, “Self-supervised learning for medical image classification: a systematic review and implementation guidelines,” *npj Digital Medicine*, vol. 6, no. 1, p. 74, 2023.
- [38] M. Nadif and F. Role, “Unsupervised and self-supervised deep learning approaches for biomedical text mining,” *Briefings in Bioinformatics*, vol. 22, no. 2, pp. 1592–1603, 2021.
- [39] R. Krishnan, P. Rajpurkar, and E. J. Topol, “Self-supervised learning in medicine and healthcare,” *Nature Biomedical Engineering*, pp. 1–7, 2022.
- [40] P. Liu, W. Yuan, J. Fu, Z. Jiang, H. Hayashi, and G. Neubig, “Pre-train, prompt, and predict: A systematic survey of prompting methods in natural language processing,” *ACM Computing Surveys*, vol. 55, no. 9, pp. 1–35, 2023.
- [41] J. Wei, M. Bosma, V. Zhao, K. Guu, A. W. Yu, B. Lester, N. Du, A. M. Dai, and Q. V. Le, “Finetuned language models are zero-shot learners,” in *International Conference on Learning Representations*, 2022.
- [42] T. Gao, A. Fisch, and D. Chen, “Making pre-trained language models better few-shot learners,” in *Proceedings of the 59th Annual Meeting of the Association for Computational Linguistics and the 11th International Joint Conference on Natural Language Processing (Volume 1: Long Papers)*, 2021, pp. 3816–3830.
- [43] T. Schick and H. Schütze, “It’s not just size that matters: Small language models are also few-shot learners,” in *Proceedings of the 2021 Conference of the North American Chapter of the Association for Computational Linguistics: Human Language Technologies*, 2021, pp. 2339–2352.
- [44] J. J. Lau, S. Gayen, A. Ben Abacha, and D. Demner-Fushman, “A dataset of clinically generated visual questions and answers about radiology images,” *Scientific data*, vol. 5, no. 1, pp. 1–10, 2018.
- [45] B. Liu, L.-M. Zhan, L. Xu, L. Ma, Y. Yang, and X.-M. Wu, “Slake: a semantically-labeled knowledge-enhanced dataset for medical visual question answering,” in *2021 IEEE 18th International Symposium on Biomedical Imaging (ISBI)*. IEEE, 2021, pp. 1650–1654.
- [46] X. He, Y. Zhang, L. Mou, E. Xing, and P. Xie, “Pathvqa: 30000+ questions for medical visual question answering,” *arXiv preprint arXiv:2003.10286*, 2020.
- [47] D. Demner-Fushman, M. D. Kohli, M. B. Rosenman, S. E. Shooshan, L. Rodriguez, S. Antani, G. R. Thoma, and C. J. McDonald, “Preparing a collection of radiology examinations for distribution and retrieval,” *Journal of the American Medical Informatics Association*, vol. 23, no. 2, pp. 304–310, 2016.
- [48] A. E. Johnson, T. J. Pollard, N. R. Greenbaum, M. P. Lungren, C.-y. Deng, Y. Peng, Z. Lu, R. G. Mark, S. J. Berkowitz, and S. Horng, “Mimic-cxr-jpg, a large publicly available database of labeled chest radiographs,” *arXiv preprint arXiv:1901.07042*, 2019.

- [49] J. Pavlopoulos, V. Kougia, and I. Androutsopoulos, "A survey on biomedical image captioning," in *Proceedings of the second workshop on shortcomings in vision and language*, 2019, pp. 26–36.
- [50] P. Li, G. Liu, L. Tan, J. Liao, and S. Zhong, "Self-supervised vision-language pretraining for medial visual question answering," in *2023 IEEE 20th International Symposium on Biomedical Imaging (ISBI)*. IEEE, 2023, pp. 1–5.
- [51] X. Zhang, C. Wu, Z. Zhao, W. Lin, Y. Zhang, Y. Wang, and W. Xie, "Pmc-vqa: Visual instruction tuning for medical visual question answering," *arXiv preprint arXiv:2305.10415*, 2023.
- [52] S. Zhang, Y. Xu, N. Usuyama, J. Bagga, R. Tinn, S. Preston, R. Rao, M. Wei, N. Valluri, C. Wong *et al.*, "Large-scale domain-specific pretraining for biomedical vision-language processing," *arXiv preprint arXiv:2303.00915*, 2023.
- [53] T. van Sonsbeek, M. M. Derakhshani, I. Najdenkoska, C. G. Snoek, and M. Worrying, "Open-ended medical visual question answering through prefix tuning of language models," *arXiv preprint arXiv:2303.05977*, 2023.
- [54] C.-Y. Lin, "Rouge: A package for automatic evaluation of summaries," in *Text summarization branches out*, 2004, pp. 74–81.
- [55] S. Banerjee and A. Lavie, "Meteor: An automatic metric for mt evaluation with improved correlation with human judgments," in *Proceedings of the acl workshop on intrinsic and extrinsic evaluation measures for machine translation and/or summarization*, 2005, pp. 65–72.
- [56] R. Vedantam, C. Lawrence Zitnick, and D. Parikh, "Cider: Consensus-based image description evaluation," in *Proceedings of the IEEE conference on computer vision and pattern recognition*, 2015, pp. 4566–4575.
- [57] N. Aafaq, A. Mian, W. Liu, S. Z. Gilani, and M. Shah, "Video description: A survey of methods, datasets, and evaluation metrics," *ACM Computing Surveys (CSUR)*, vol. 52, no. 6, pp. 1–37, 2019.
- [58] B. Jing, P. Xie, and E. Xing, "On the automatic generation of medical imaging reports," in *Proceedings of the 56th Annual Meeting of the Association for Computational Linguistics (Volume 1: Long Papers)*, 2018, pp. 2577–2586.
- [59] Z. Chen, Y. Song, T.-H. Chang, and X. Wan, "Generating radiology reports via memory-driven transformer," in *Proceedings of the 2020 Conference on Empirical Methods in Natural Language Processing (EMNLP)*, 2020, pp. 1439–1449.
- [60] F. Liu, X. Wu, S. Ge, W. Fan, and Y. Zou, "Exploring and distilling posterior and prior knowledge for radiology report generation," in *Proceedings of the IEEE/CVF Conference on Computer Vision and Pattern Recognition*, 2021, pp. 13 753–13 762.
- [61] J. Yang, R. Shi, D. Wei, Z. Liu, L. Zhao, B. Ke, H. Pfister, and B. Ni, "Medmnist v2: A large-scale lightweight benchmark for 2d and 3d biomedical image classification," *arXiv preprint arXiv:2110.14795*, 2021.
- [62] S. Jaeger, S. Candemir, S. Antani, Y.-X. J. Wang, P.-X. Lu, and G. Thoma, "Two public chest x-ray datasets for computer-aided screening of pulmonary diseases," *Quantitative imaging in medicine and surgery*, vol. 4, no. 6, p. 475, 2014.
- [63] D. Capellán-Martín, J. J. Gómez-Valverde, D. Bermejo-Peláez, and M. J. Ledesma-Carbayo, "A lightweight, rapid and efficient deep convolutional network for chest x-ray tuberculosis detection," in *2023 IEEE 20th International Symposium on Biomedical Imaging (ISBI)*. IEEE, 2023, pp. 1–5.
- [64] R. S. Lee, F. Gimenez, A. Hoogi, K. K. Miyake, M. Gorovoy, and D. L. Rubin, "A curated mammography data set for use in computer-aided detection and diagnosis research," *Scientific data*, vol. 4, no. 1, pp. 1–9, 2017.
- [65] A. Romanov and C. Shivade, "Lessons from natural language inference in the clinical domain," in *Proceedings of the 2018 Conference on Empirical Methods in Natural Language Processing*, 2018, pp. 1586–1596.

- [66] A. B. Abacha and D. Demner-Fushman, "On the summarization of consumer health questions," in *Proceedings of the 57th Annual Meeting of the Association for Computational Linguistics*, 2019, pp. 2228–2234.
- [67] G. Zeng, W. Yang, Z. Ju, Y. Yang, S. Wang, R. Zhang, M. Zhou, J. Zeng, X. Dong, R. Zhang *et al.*, "Meddialog: Large-scale medical dialogue datasets," in *Proceedings of the 2020 Conference on Empirical Methods in Natural Language Processing (EMNLP)*, 2020, pp. 9241–9250.
- [68] A. E. Johnson, T. J. Pollard, L. Shen, L.-w. H. Lehman, M. Feng, M. Ghassemi, B. Moody, P. Szolovits, L. Anthony Celi, and R. G. Mark, "Mimic-iii, a freely accessible critical care database," *Scientific data*, vol. 3, no. 1, pp. 1–9, 2019.
- [69] C. Raffel, N. Shazeer, A. Roberts, K. Lee, S. Narang, M. Matena, Y. Zhou, W. Li, P. J. Liu *et al.*, "Exploring the limits of transfer learning with a unified text-to-text transformer." *J. Mach. Learn. Res.*, vol. 21, no. 140, pp. 1–67, 2020.
- [70] M. Lewis, Y. Liu, N. Goyal, M. Ghazvininejad, A. Mohamed, O. Levy, V. Stoyanov, and L. Zettlemoyer, "Bart: Denoising sequence-to-sequence pre-training for natural language generation, translation, and comprehension," *arXiv preprint arXiv:1910.13461*, 2019.
- [71] H. Yuan, Z. Yuan, R. Gan, J. Zhang, Y. Xie, and S. Yu, "Biobart: Pretraining and evaluation of a biomedical generative language model," in *Proceedings of the 21st Workshop on Biomedical Language Processing*, 2022, pp. 97–109.
- [72] O. Pelka, S. Koitka, J. Rückert, F. Nensa, and C. M. Friedrich, "Radiology objects in context (roco): a multimodal image dataset," in *Intravascular Imaging and Computer Assisted Stenting and Large-Scale Annotation of Biomedical Data and Expert Label Synthesis*. Springer, 2018, pp. 180–189.
- [73] K. He, X. Zhang, S. Ren, and J. Sun, "Deep residual learning for image recognition," in *Proceedings of the IEEE conference on computer vision and pattern recognition*, 2016, pp. 770–778.
- [74] C. H. Lampert, H. Nickisch, and S. Harmeling, "Learning to detect unseen object classes by between-class attribute transfer," in *2009 IEEE conference on computer vision and pattern recognition*. IEEE, 2009, pp. 951–958.
- [75] M. Palatucci, D. Pomerleau, G. E. Hinton, and T. M. Mitchell, "Zero-shot learning with semantic output codes," *Advances in neural information processing systems*, vol. 22, 2009.
- [76] L. Ouyang, J. Wu, X. Jiang, D. Almeida, C. Wainwright, P. Mishkin, C. Zhang, S. Agarwal, K. Slama, A. Ray *et al.*, "Training language models to follow instructions with human feedback," *Advances in Neural Information Processing Systems*, vol. 35, pp. 27 730–27 744, 2022.
- [77] Z. Huang, F. Bianchi, M. Yuksekogonul, T. J. Montine, and J. Zou, "A visual–language foundation model for pathology image analysis using medical twitter," *Nature medicine*, vol. 29, no. 9, pp. 2307–2316, 2023.
- [78] L. Zhou, H. Liu, J. Bae, J. He, D. Samaras, and P. Prasanna, "Self pre-training with masked autoencoders for medical image classification and segmentation," in *2023 IEEE 20th International Symposium on Biomedical Imaging (ISBI)*. IEEE, 2023, pp. 1–6.
- [79] S. Chakraborty, E. Bisong, S. Bhatt, T. Wagner, R. Elliott, and F. Mosconi, "Biomedbert: A pre-trained biomedical language model for qa and ir," in *Proceedings of the 28th International Conference on Computational Linguistics*, 2020, pp. 669–679.
- [80] O. N. Manzari, H. Ahmadabadi, H. Kashiani, S. B. Shokouhi, and A. Ayatollahi, "Medvit: A robust vision transformer for generalized medical image classification," *Computers in Biology and Medicine*, vol. 157, p. 106791, 2023.
- [81] J. Lee, W. Yoon, S. Kim, D. Kim, S. Kim, C. H. So, and J. Kang, "Biobert: a pre-trained biomedical language representation model for biomedical text mining," *Bioinformatics*, vol. 36, no. 4, pp. 1234–1240, 2020.

- [82] E. Alsentzer, J. R. Murphy, W. Boag, W.-H. Weng, D. Jin, T. Naumann, W. Redmond, and M. B. McDermott, "Publicly available clinical bert embeddings," *NAACL HLT 2019*, p. 72, 2019.
- [83] G. Alain and Y. Bengio, "Understanding intermediate layers using linear classifier probes," 2017. [Online]. Available: <https://openreview.net/forum?id=ryF7rTqgl>
- [84] Y. Zhang, H. Jiang, Y. Miura, C. D. Manning, and C. P. Langlotz, "Contrastive learning of medical visual representations from paired images and text," in *Machine Learning for Healthcare Conference*. PMLR, 2022, pp. 2–25.
- [85] S.-C. Huang, L. Shen, M. P. Lungren, and S. Yeung, "Gloria: A multimodal global-local representation learning framework for label-efficient medical image recognition," in *Proceedings of the IEEE/CVF International Conference on Computer Vision*, 2021, pp. 3942–3951.
- [86] Z. Wang, Z. Wu, D. Agarwal, and J. Sun, "MedCLIP: Contrastive learning from unpaired medical images and text," in *Proceedings of the 2022 Conference on Empirical Methods in Natural Language Processing*. Abu Dhabi, United Arab Emirates: Association for Computational Linguistics, Dec. 2022, pp. 3876–3887.
- [87] S. Eslami, C. Meinel, and G. De Melo, "Pubmedclip: How much does clip benefit visual question answering in the medical domain?" in *Findings of the Association for Computational Linguistics: EACL 2023*, 2023, pp. 1151–1163.
- [88] Z. Yan, K. Zhang, R. Zhou, L. He, X. Li, and L. Sun, "Multimodal chatgpt for medical applications: an experimental study of gpt-4v," *arXiv preprint arXiv:2310.19061*, 2023.
- [89] S. Bubeck, V. Chandrasekaran, R. Eldan, J. Gehrke, E. Horvitz, E. Kamar, P. Lee, Y. T. Lee, Y. Li, S. Lundberg *et al.*, "Sparks of artificial general intelligence: Early experiments with gpt-4," *arXiv preprint arXiv:2303.12712*, 2023.
- [90] X. Hu, L. Gu, Q. An, M. Zhang, L. Liu, K. Kobayashi, T. Harada, R. M. Summers, and Y. Zhu, "Expert knowledge-aware image difference graph representation learning for difference-aware medical visual question answering," in *Proceedings of the 29th ACM SIGKDD Conference on Knowledge Discovery and Data Mining*, 2023, pp. 4156–4165.
- [91] S. Fu, A. Wen, G. M. Schaeferle, P. M. Wilson, G. Demuth, X. Ruan, S. Liu, C. Storlie, and H. Liu, "Assessment of data quality variability across two ehr systems through a case study of post-surgical complications," in *AMIA Annual symposium proceedings*, vol. 2022. American Medical Informatics Association, 2022, p. 196.
- [92] S. Wang, C. Li, R. Wang, Z. Liu, M. Wang, H. Tan, Y. Wu, X. Liu, H. Sun, R. Yang *et al.*, "Annotation-efficient deep learning for automatic medical image segmentation," *Nature communications*, vol. 12, no. 1, p. 5915, 2021.
- [93] J.-B. Delbrouck, P. Chambon, C. Bluethgen, E. Tsai, O. Almusa, and C. Langlotz, "Improving the factual correctness of radiology report generation with semantic rewards," in *Findings of the Association for Computational Linguistics: EMNLP 2022*, 2022, pp. 4348–4360.
- [94] S. Jain, A. Agrawal, A. Saporta, S. Truong, T. Bui, P. Chambon, Y. Zhang, M. P. Lungren, A. Y. Ng, C. Langlotz *et al.*, "Radgraph: Extracting clinical entities and relations from radiology reports," in *Thirty-fifth Conference on Neural Information Processing Systems Datasets and Benchmarks Track (Round 1)*, 2021.
- [95] Y. Zhang, D. Merck, E. Tsai, C. D. Manning, and C. Langlotz, "Optimizing the factual correctness of a summary: A study of summarizing radiology reports," in *Proceedings of the 58th Annual Meeting of the Association for Computational Linguistics*, 2020, pp. 5108–5120.
- [96] D. Ouyang, B. He, A. Ghorbani, N. Yuan, J. Ebinger, C. P. Langlotz, P. A. Heidenreich, R. A. Harrington, D. H. Liang, E. A. Ashley *et al.*, "Video-based ai for beat-to-beat assessment of cardiac function," *Nature*, vol. 580, no. 7802, pp. 252–256, 2020.

- [97] S. Kim, K. Kim, J. Hu, C. Chen, Z. Lyu, R. Hui, S. Kim, Z. Liu, A. Zhong, X. Li *et al.*, “Medivista-sam: Zero-shot medical video analysis with spatio-temporal sam adaptation,” *arXiv preprint arXiv:2309.13539*, 2023.
- [98] X. Ruan, S. Fu, C. B. Storlie, K. L. Mathis, D. W. Larson, and H. Liu, “Real-time risk prediction of colorectal surgery-related post-surgical complications using gru-d model,” *Journal of Biomedical Informatics*, vol. 135, p. 104202, 2022.
- [99] Y. Gorishniy, I. Rubachev, V. Khruikov, and A. Babenko, “Revisiting deep learning models for tabular data,” *Advances in Neural Information Processing Systems*, vol. 34, pp. 18 932–18 943, 2021.
- [100] J. Selva, A. S. Johansen, S. Escalera, K. Nasrollahi, T. B. Moeslund, and A. Clapés, “Video transformers: A survey,” *IEEE Transactions on Pattern Analysis and Machine Intelligence*, 2023.
- [101] Q. Wen, T. Zhou, C. Zhang, W. Chen, Z. Ma, J. Yan, and L. Sun, “Transformers in time series: A survey,” *arXiv preprint arXiv:2202.07125*, 2022.
- [102] R. A. Jacobs, M. I. Jordan, S. J. Nowlan, and G. E. Hinton, “Adaptive mixtures of local experts,” *Neural computation*, vol. 3, no. 1, pp. 79–87, 1991.
- [103] K. Meng, D. Bau, A. Andonian, and Y. Belinkov, “Locating and editing factual associations in gpt,” *Advances in Neural Information Processing Systems*, vol. 35, pp. 17 359–17 372, 2022.
- [104] N. Ding, Y. Qin, G. Yang, F. Wei, Z. Yang, Y. Su, S. Hu, Y. Chen, C.-M. Chan, W. Chen *et al.*, “Parameter-efficient fine-tuning of large-scale pre-trained language models,” *Nature Machine Intelligence*, pp. 1–16, 2023.
- [105] H. Liu, D. Tam, M. Muqeeth, J. Mohta, T. Huang, M. Bansal, and C. A. Raffel, “Few-shot parameter-efficient fine-tuning is better and cheaper than in-context learning,” *Advances in Neural Information Processing Systems*, vol. 35, pp. 1950–1965, 2022.
- [106] V. Lialin, V. Deshpande, and A. Rumshisky, “Scaling down to scale up: A guide to parameter-efficient fine-tuning,” *arXiv preprint arXiv:2303.15647*, 2023.
- [107] H. Yang, J. Lin, A. Yang, P. Wang, and C. Zhou, “Prompt tuning for unified multimodal pretrained models,” in *Findings of the Association for Computational Linguistics: ACL 2023*, 2023, pp. 402–416.
- [108] E. J. Hu, yelong shen, P. Wallis, Z. Allen-Zhu, Y. Li, S. Wang, L. Wang, and W. Chen, “LoRA: Low-rank adaptation of large language models,” in *International Conference on Learning Representations*, 2022. [Online]. Available: <https://openreview.net/forum?id=nZeVKeeFYf9>
- [109] T. Dettmers, A. Pagnoni, A. Holtzman, and L. Zettlemoyer, “Qlora: Efficient finetuning of quantized llms,” *arXiv preprint arXiv:2305.14314*, 2023.
- [110] A. Dosovitskiy, L. Beyer, A. Kolesnikov, D. Weissenborn, X. Zhai, T. Unterthiner, M. Dehghani, M. Minderer, G. Heigold, S. Gelly *et al.*, “An image is worth 16x16 words: Transformers for image recognition at scale,” *arXiv preprint arXiv:2010.11929*, 2020.
- [111] M. Lewis, Y. Liu, N. Goyal, M. Ghazvininejad, A. Mohamed, O. Levy, V. Stoyanov, and L. Zettlemoyer, “BART: Denoising sequence-to-sequence pre-training for natural language generation, translation, and comprehension,” in *Proceedings of the 58th Annual Meeting of the Association for Computational Linguistics*. Online: Association for Computational Linguistics, Jul. 2020, pp. 7871–7880. [Online]. Available: <https://aclanthology.org/2020.acl-main.703>
- [112] G. Ke, D. He, and T.-Y. Liu, “Rethinking positional encoding in language pre-training,” in *International Conference on Learning Representations*, 2019.
- [113] J. L. Ba, J. R. Kiros, and G. E. Hinton, “Layer normalization,” *arXiv preprint arXiv:1607.06450*, 2016.
- [114] S. Shleifer, J. Weston, and M. Ott, “Normformer: Improved transformer pretraining with extra normalization,” *arXiv preprint arXiv:2110.09456*, 2021.

- [115] N. Kitaev and D. Klein, “Constituency parsing with a self-attentive encoder,” in *Proceedings of the 56th Annual Meeting of the Association for Computational Linguistics (Volume 1: Long Papers)*, 2018, pp. 2676–2686.
- [116] Z. Dai, H. Liu, Q. V. Le, and M. Tan, “Coatnet: Marrying convolution and attention for all data sizes,” *Advances in Neural Information Processing Systems*, vol. 34, pp. 3965–3977, 2021.
- [117] Z. Wang, J. Yu, A. W. Yu, Z. Dai, Y. Tsvetkov, and Y. Cao, “Simvlm: Simple visual language model pretraining with weak supervision,” in *International Conference on Learning Representations*, 2022.
- [118] A. Van Den Oord, O. Vinyals *et al.*, “Neural discrete representation learning,” *Advances in neural information processing systems*, vol. 30, 2017.
- [119] P. Esser, R. Rombach, and B. Ommer, “Taming transformers for high-resolution image synthesis,” in *Proceedings of the IEEE/CVF conference on computer vision and pattern recognition*, 2021, pp. 12 873–12 883.
- [120] T. Chen, S. Saxena, L. Li, D. J. Fleet, and G. Hinton, “Pix2seq: A language modeling framework for object detection,” in *International Conference on Learning Representations*, 2022. [Online]. Available: <https://openreview.net/forum?id=e42Kblw6Wb>
- [121] T. Chen, S. Saxena, L. Li, T.-Y. Lin, D. J. Fleet, and G. E. Hinton, “A unified sequence interface for vision tasks,” *Advances in Neural Information Processing Systems*, vol. 35, pp. 31 333–31 346, 2022.
- [122] H. Bao, L. Dong, and F. Wei, “Beit: Bert pre-training of image transformers,” *arXiv preprint arXiv:2106.08254*, 2021.
- [123] A. Kuznetsova, H. Rom, N. Alldrin, J. Uijlings, I. Krasin, J. Pont-Tuset, S. Kamali, S. Popov, M. Mallocci, A. Kolesnikov *et al.*, “The open images dataset v4: Unified image classification, object detection, and visual relationship detection at scale,” *International Journal of Computer Vision*, vol. 128, no. 7, pp. 1956–1981, 2020.
- [124] E. Jang, S. Gu, and B. Poole, “Categorical reparameterization with gumbel-softmax,” in *International Conference on Learning Representations*, 2017.
- [125] C. J. Maddison, A. Mnih, and Y. W. Teh, “The concrete distribution: A continuous relaxation of discrete random variables,” in *International Conference on Learning Representations*, 2017.
- [126] H. Bao, L. Dong, S. Piao, and F. Wei, “Beit: BERT pre-training of image transformers,” in *The Tenth International Conference on Learning Representations, ICLR 2022, Virtual Event, April 25-29, 2022*. OpenReview.net, 2022. [Online]. Available: <https://openreview.net/forum?id=p-BhZSz59o4>
- [127] H. Xu, M. Yan, C. Li, B. Bi, S. Huang, W. Xiao, and F. Huang, “E2e-vlp: End-to-end vision-language pre-training enhanced by visual learning,” in *Proceedings of the 59th Annual Meeting of the Association for Computational Linguistics and the 11th International Joint Conference on Natural Language Processing (Volume 1: Long Papers)*, 2021, pp. 503–513.
- [128] I. Sutskever, O. Vinyals, and Q. V. Le, “Sequence to sequence learning with neural networks,” *Advances in neural information processing systems*, vol. 27, 2014.
- [129] K. Cho, B. van Merriënboer, C. Gulcehre, D. Bahdanau, F. Bougares, H. Schwenk, and Y. Bengio, “Learning phrase representations using RNN encoder–decoder for statistical machine translation,” in *Proceedings of the 2014 Conference on Empirical Methods in Natural Language Processing (EMNLP)*. Doha, Qatar: Association for Computational Linguistics, Oct. 2014, pp. 1724–1734. [Online]. Available: <https://aclanthology.org/D14-1179>
- [130] A. v. d. Oord, S. Dieleman, H. Zen, K. Simonyan, O. Vinyals, A. Graves, N. Kalchbrenner, A. Senior, and K. Kavukcuoglu, “Wavenet: A generative model for raw audio,” *arXiv preprint arXiv:1609.03499*, 2016.
- [131] I. Loshchilov and F. Hutter, “Decoupled weight decay regularization,” in *International Conference on Learning Representations*, 2019.

- [132] P. Micikevicius, S. Narang, J. Alben, G. Damos, E. Elsen, D. Garcia, B. Ginsburg, M. Houston, O. Kuchaiev, G. Venkatesh, and H. Wu, "Mixed precision training," in *International Conference on Learning Representations*, 2018. [Online]. Available: <https://openreview.net/forum?id=r1gs9JgRZ>
- [133] M. Raghu, C. Zhang, J. Kleinberg, and S. Bengio, "Transfusion: Understanding transfer learning for medical imaging," *Advances in neural information processing systems*, vol. 32, 2019.
- [134] S. Niu, M. Liu, Y. Liu, J. Wang, and H. Song, "Distant domain transfer learning for medical imaging," *IEEE Journal of Biomedical and Health Informatics*, vol. 25, no. 10, pp. 3784–3793, 2021.

Extended Tables and Figures

Extended Table 1: Fine-tuned experimental results of BiomedGPT on 25 diverse datasets. For comparison, we list the performance of the SOTA approaches. The *star* shown in the table indicates the result that outperforms the previous SOTAs

Task	Dataset	Domain / Modality	Metric	SOTA		BiomedGPT		
				Model	Result	Small	Medium	Base
Image classification	MedMNIST	Colon pathology	Accuracy	MedViT-S (224)	94.2	89.4	92.1	92.6
		Dermatoscope		PMC-CLIP	79.8	75.2	78.0	78.6
		Retinal OCT 🌟		MedViT-S (224)	78.2	79.5	81.9	81.6
		Chest X-Ray 🌟		MedViT-S (224)	96.1	91.8	93.4	96.7
		Breast Ultrasound		PMC-CLIP	91.3	84.6	87.8	87.8
		Blood Cell Microscope 🌟		AutoML	96.6	94.2	97.2	97.7
		Axial Abdominal CT 🌟		ResNet-18 (224)	95.1	92.6	94.7	95.2
		Coronal Abdominal CT 🌟		MedViT-L (224)	92.2	92.2	92.3	93.1
		Sagittal Abdominal CT 🌟		AutoKeras	81.3	80.0	82.0	82.3
	MC-CXR 🌟	Chest X-Ray	LightTBNNet	88.9	75.9	82.8	89.7	
	SZ-CXR 🌟	Chest X-Ray		91.0	83.5	97.0	96.2	
	CBIS-DDSM	Mass 🌟	F1-Macro	Med-PaLM M (562B)	51.1	-	18.7	57.2
Calcification 🌟		Med-PaLM M (12B)		67.9	-	18.9	72.8	
Text understanding	MedNLI	Clinic notes	Accuracy	SciFive	85.6	75.8	80.8	83.8
Text Summarization	MeQSum	Doctor-patient dialogues	ROUGEL-L	BioBART-L	53.2	42.2	51.3	52.3
	HealthCareMagic	Doctor-patient dialogues	ROUGEL-L	BART-L	44.7	39.8	41.99	42.0
	MIMC-CXR 🌟	Radiology report	ROUGEL-L	RadAdapt	44.5	-	-	44.4
			F1-RadGraph	RadAdapt	41.8	-	-	45.1
	MIMIC-III	Radiology report	ROUGEL-L	MedPaLM M (562B)	32.0	-	-	30.7
F1-RadGraph			MedPaLM M (562B)	34.7	-	-	31.2	
Visual question answering	PathVQA	Pathology	Accuracy	CLIP-ViT w/ GPT2	63.6	47.6	49.2	58.1
	VQA-RAD	Radiology		MedViT-TD	81.6	40.1	69.4	73.2
	SLAKE 🌟	Radiology		BiomedCLIP	85.4	69.2	81.6	86.1
Image captioning	IU X-RAY 🌟	Chest X-Ray	CIDEr	PPKED	35.1	29.6	31.3	40.1
	PEIR GROSS 🌟	Digital camera		CoAttention	32.9	22.0	25.8	122.7
	MIMIC-CXR	Radiology		MedPaLM M (84B)	26.2	-	-	14.7
	ROCO 🌟	Mixed	METEOR	N/A	N/A	6.2	7.0	7.8
			ROUGEL-L	N/A	N/A	16.4	17.0	18.2
CIDEr			N/A	N/A	13.2	17.6	24.2	

Extended Table 2: Instructions for pretraining tasks along with the corresponding format of the output. Here, ** represents the image token derived from VQ-GAN’s vocabulary. *<loc>* represents the location token. The instruction for visual question answering task is the question itself from the dataset.

Task	Instructions	The example of output
Masked image modeling	What is the image in the middle part?	<img111> <img222> <img333> ... <img999>
Masked language modeling	What is the complete text of "Effect of <mask> on cultured fibroblasts" ?	Effect of chloroquine on cultured fibroblasts
Object detection	What are the objects in the image?	<loc111> <123> <loc789> <loc567> chest <loc222> <333> <loc666> <loc999> kidney
Image captioning	What does the image describe?	Interval placement of endotracheal tube and nasogastric tube in standard position.
Visual question answering	{Question}	{Answer}

Extended Table 3: Description of the questions types in the selected VQA-RAD data samples, which are used for the evaluation of zero-shot learning performance.

Type	Explanation
Modality recognition	The specific imaging modality, such as CT, MRI, or others.
Structural identification	The specific anatomical landmarks or structures within the captured images.
Lesion & abnormality detection	The identification of anomalous patterns or aberrations
Disease diagnosis	Specific disease or medical conditions based on imaging manifestations
Size & extent assessment	The dimensions and spread of a lesion or abnormality.
Spatial relationships	The relative positioning or orientation of imaged structures.
Image technical details	The nuances of the imaging process itself, such as contrast utilization or image orientation

Extended Table 4: Detailed model configuration of BiomedGPT. Here, ‘#’ indicates *number of*. ‘Att.’, ‘Enc.’ and ‘Dec.’ indicate *Attention, Encoder* and *Decoder*, respectively. The hidden size is the size of the embeddings and the size of the output of each self-attention and feed-forward layer. The first layer of FFN expands the hidden size to the intermediate size, and the second layer contracts it back to the hidden size. This expansion and contraction allow the network to create more complex representations. During the pretraining phase, image processing involves resizing and cropping the images to varying resolutions, corresponding to the input sizes listed in the table. It should be noted that during fine-tuning and inference stages, the input resolution of BiomedGPT can be flexibly adjusted according to the specific requirements of the task.

Model scale	#Parameters	Image projection		Representation size		Transformer block		
		Input size	Visual encoder	Hidden	Intermediate	Att. head	#Enc. layer	#Dec. layer
BiomedGPT-S	33 million	256 × 256	ResNet-50	256	1024	4	4	4
BiomedGPT-M	93 million	256 × 256	ResNet-101	512	2048	8	4	4
BiomedGPT-B	182 million	256 × 256	ResNet-101	768	3072	12	6	6

Extended Table 5: Details of the selected VQA-RAD data samples for zero-shot evaluation. The image names are derived from the original dataset.

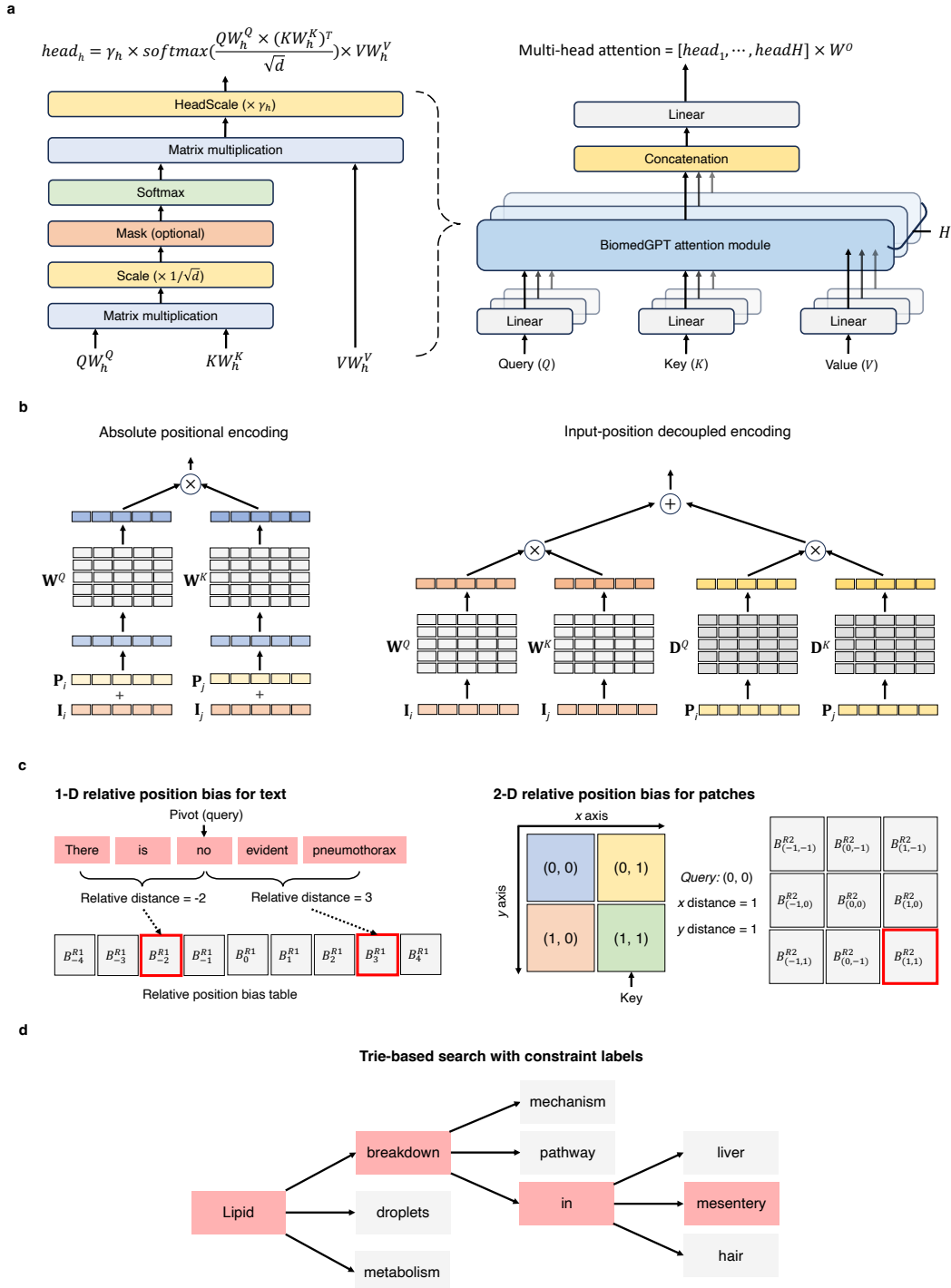
Experiment ID	Image name	Question	Gold answer
1	synpic28602	What type of imaging does this not represent?	Ultrasound
2	synpic29265	Is this a MRI of the chest?	No
3	synpic54610	What type of imaging is this?	MRI Diffusion Weighted
4	synpic42202	What type of image is this?	Chest X-ray
5	synpic39460	Is this a CT image?	No
6	synpic20260	What kind of scan is this?	CT
7	synpic34854	What type of MRI sequence is this?	Diffusion Weighted Imaging (DWI)
8	synpic17153	What type of MRI is used to acquire this image?	T2-Weighted
9	synpic28602	What is not pictured in this image?	The extremities
10	synpic16520	In which two ventricles can calcifications be seen on this CT scan?	The 3rd ventricle and the lateral ventricles
11	synpic19605	Is the celiac trunk visualized and patent?	Yes
12	synpic40314	Which organ has the abnormality?	Pancreas
13	synpic53228	How many ribs are superimposed on the lung fields?	12
14	synpic22791	How many kidneys are visualizable in this image?	Two
15	synpic28602	Is there evidence of an aortic aneurysm?	No
16	synpic28602	Is there blunting of the costovertebral angles?	No
17	synpic16520	Is there acute blood present on this head CT?	No
18	synpic19605	Is the liver parenchyma normal?	Yes
19	synpic19605	Is there no evidence of any hypo- or hyperattenuations located in the liver?	Yes
20	synpic39460	Where is the abnormality?	Left temporal lobe
21	synpic40464	How many lesions are in the spleen?	One
22	synpic19605	Are the structures in the pancreas cystic or solid?	Cystic
23	synpic33689	How would you describe the duodenum?	Edematous
24	synpic31916	How do we call these wide undulations along the vertebral column?	Scoliosis
25	synpic19605	Is the size of the spleen normal?	Yes
26	synpic16174	Is the descending aortic silhouette of normal contour and size?	Yes
27	synpic22967	Is the gallbladder large in size?	No
28	synpic22967	Is the gallbladder distended?	No
29	synpic42245	Are the soft tissue densities in the left hilum equivalent in size to the soft tissue densities in the right hilum?	No
30	synpic16174	Is the cardiac silhouette less than half the diameter of the diaphragm?	Yes
31	synpic16174	Are/s the heart size normal?	Yes
32	synpic21776	Is there narrowing of the cardiac contour?	Yes
33	synpic22286	Is the gallbladder enlarged?	Yes
34	synpic39088	Is there enlargement of the abdominal aorta on this image?	No
35	synpic46720	Is there atrophy of the brain?	Yes
36	synpic28602	Is the trachea midline?	Yes
37	synpic28602	Is this an anterior posterior image?	No
38	synpic16520	Is this a contrast CT or a non-contrast CT?	No-contrast CT
39	synpic33689	Was oral or IV contrast used?	Both

Extended Table 6: Generated answers from BiomedGPT in zero-shot prediction. The red texts indicate that the answer does not align with the question. Additionally, <image tokens> were utilized to indicate instances where the output was represented by a patch token from BiomedGPT's unified vocabulary instead of freeform text.

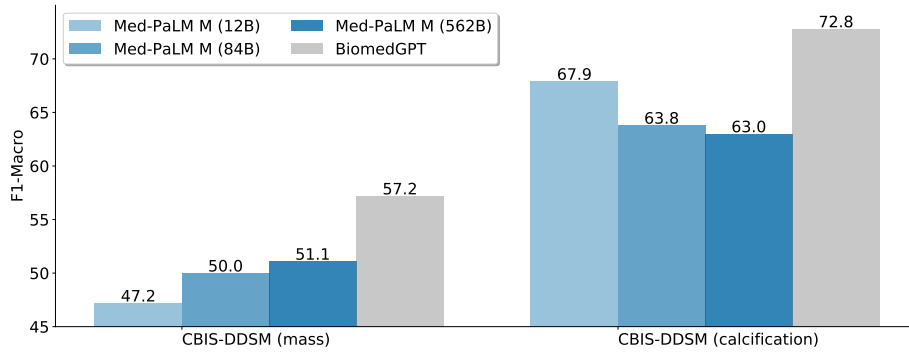
Experiment ID	BiomedGPT-B	BiomedGPT-M	BiomedGPT-S
1	x-ray	aortic x-ray appearance	a
2	no	yes	no
3	<image tokens>	diffusion weighted imaging	coronal t2 weighted mri
4	x-ray	x-ray	a soft tissue
5	no	no	no
6	CT scan	CT	liver
7	covered right lateral ventricle	diffusion weighted mri sequence	bone bone
8	MRI	T2	T1
9	Lung	x-ray chest with obvious cardiomegaly	aortic valve
10	no	""	heart
11	yes	no	no
12	abdomen	liver	heart
13	2	2	a
14	2	2	two
15	yes	yes	yes
16	no	yes	yes
17	no	no	no
18	yes	yes	no
19	liver	liver	no
20	lower right	lower left	left left
21	2	2	2
22	liver	no	no
23	good	""	a ct scan of the abdomen and pelvis showing a large, well defined, lobulated mass in the right lower quadrant of the abdomen.
24	hilar lymphadenopathy	with a wide field light field	a few
25	yes	yes	no
26	no	no	yes
27	yes	no	yes
28	yes	no	yes
29	no	yes	yes
30	yes	yes	yes
31	yes	yes	yes
32	yes	yes	yes
33	yes	yes	yes
34	no	no	yes
35	no	yes	there is a large mass in the left parietal lobe
36	yes	yes	yes
37	no	yes	yes
38	noncontrast ct cranial to the brain	no	yes
39	iotomography	no	yes

Extended Table 7: Generated answers from OFL-L and OFA-B in zero-shot prediction. The red texts indicate that the answer does not align with the question.

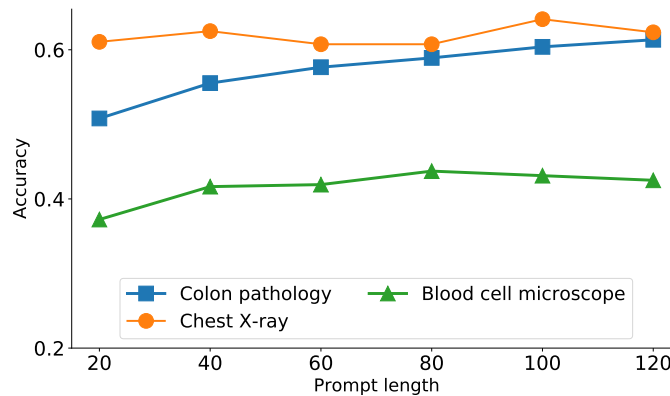
Experiment ID	OFA-L	OFA-B
1	xray	chest
2	yes	yes
3	mri	ct
4	black and white	chest
5	yes	yes
6	mri	mri
7	brain	mri
8	mri	mri
9	skull	the left ventricle
10	no	right
11	yes	no
12	brain	the middle
13	6	2
14	3	one
15	no	yes
16	yes	no
17	no	yes
18	no	no
19	yes	yes
20	in the middle of the mri	in the brain
21	2	2
22	solid	cystic
23	normal	it is a black and white image of a normal human stomach
24	they are called wide undulations	ribs
25	no	no
26	yes	yes
27	no	yes
28	yes	yes
29	no	yes
30	yes	yes
31	yes	yes
32	yes	yes
33	yes	yes
34	yes	yes
35	yes	no
36	no	yes
37	no	no
38	non contrast ct	non contrast
39	iv	high contrast



Extended Figure 1: The descriptions of the key components in BiomedGPT. **(a)** Head-scale multi-head attention module in BiomedGPT. The trainable parameters γ_h is applied prior to the output projection for each head. **(b)** Instead of adding the absolute positional embedding P_i to the input embedding I_i (left), we compute the positional correlation and input correlation separately with different projection matrices, and add them together in the self-attention module (right). **(c)** Graphical illustration of relative position bias. Such an inductive bias B_{j-i} is learnable parameter and can be viewed as the embedding of the relative position $j - i$, which is injected into the Query-Key product: $\frac{1}{\sqrt{d}}(I_i W^Q)(P_i W^K) + B_{j-i}$, and shared in all layers. **(d)** An example of trie-based beam search: along the path across “Lipid” and “breakdown”, BiomedGPT sets logits for all invalid tokens (“mechanism” and “pathway”) to $-\infty$ when computing log-probabilities for the target token “in”. It is worth noting that trie-based search is also applied during the validation phase of the fine-tuning stage for acceleration (approximately $16\times$ increase in speed in our experiments)



Extended Figure 2: Comparison between BiomedGPT-B and Med-PaLM M on CBIS-DDSM dataset.



Extended Figure 3: The experimental results of prompt tuning BiomedGPT-B on three image classification datasets. Prompt tuning learns “soft prompts” or extra model parameters for each task instead of making a task-specific copy of the entire pre-trained model for each downstream task and inference must be performed in separate batches. We must mention that the addition of soft prompts is contrary to the design principle of the generalist model. We injected two prompt layers into the encoder and decoder, respectively following [107], and varied the prompt length {20, 40, 60, 80, 100, 120} to investigate the performance comparison against full-model fine-tuning. The preliminary results of ‘Colon pathology’, ‘Blood cell microscope’, and ‘Chest X-ray’ were obtained after 100, 512, and 55 training epochs respectively, all with a consistent batch size of 512. We observed that as the prompt length increases, the model performance tends to improve. However, despite an increased number of tuning epochs compared with fine-tuning on the original BiomedGPT (Fig. 3a), the performance after prompt tuning significantly lags behind that of model fine-tuning. Specifically, considering only the best results in prompt tuning, there are substantial accuracy reductions of 32.3%, 54.6%, and 32.6% on these three datasets, respectively.